Atmos. Meas. Tech. Discuss., doi:10.5194/amt-2016-20, 2016
Manuscript under review for journal Atmos. Meas. Tech.
Published: 15 February 2016

Atmospheric Measurement Techniques Discussions

A multi-wavelength classification method for polar stratospheric cloud types using infrared limb spectra

R. Spang[1], L. Hoffmann[2], M. Höpfner[3], S. Griessbach[2], R. Müller[1], M. C. Pitts[4], A. M. W. Orr[5], and M. Riese[1]

[1]Forschungszentrum Jülich, Institut für Energie und Klimaforschung, Stratosphäre, IEK-7, Jülich, Germany
[2]Forschungszentrum Jülich, Jülich Supercomputing Centre, JSC, Jülich, Germany
[3]Karlsruhe Institut für Technologie, Institut für Meteorologie und Klimaforschung, Karlsruhe, Germany
[4]NASA Langley Research Center, Hampton, VA, USA
[5]British Antarctic Survey, Cambridge, UK

Correspondence to: R. Spang (r.spang@fz-juelich.de)

Abstract. The MIPAS instrument onboard the ESA Envisat satellite operated from July 2002 until April 2012. The infrared limb emission measurements represent a unique dataset of day and night observations of polar stratospheric clouds (PSCs) up to both poles. Cloud detection sensitivity is comparable to spaceborne lidars, and it is possible to classify different cloud types from the spectral measurements in different atmospheric windows regions.

Here we present a new PSC classification scheme based on the combination of a well-established two-colour ratio method and multiple 2D brightness temperature difference probability density functions. The method is a simple probabilistic classifier based on Bayes' theorem with a strong independence assumption. The method has been tested in conjunction with a database of radiative transfer model calculations of realistic PSC particle size distributions, geometries, and composition. The Bayesian classifier distinguishes between solid particles of ice and nitric acid trihydrate (NAT), as well as liquid droplets of super-cooled ternary solution (STS).

The classification results are compared to coincident measurements from the space borne lidar CALIOP instrument over the temporal overlap of both satellite missions (June 2006 to March 2012). Both datasets show a good agreement for the specific PSC classes, although the viewing geometries, vertical and horizontal resolution are quite different. Discrepancies are observed for the MIPAS ice class. The Bayesian classifier for MIPAS identifies substantially more ice clouds in the southern hemisphere polar vortex than CALIOP. This disagreement is attributed in parts to the difference in the sensitivity on mixed-type clouds. Ice seems to dominate the spectral behaviour in the limb infrared spectra and may cause an overestimation in ice occurrence compared to the real fraction of ice within the PSC area in the polar vortex.

The entire MIPAS measurement period was processed with the new classification approach. Examples like the detection of the Antarctic NAT belt during early winter, and its possible link to mountain wave events over the Antarctic Peninsula, which are observed by the AIRS instrument, are highlighting the importance of a climatology of in total 9 southern and 10 northern hemisphere winters. The new dataset is valuable both for detailed process studies, and for comparisons with and improvements of the PSC parameterisations used in chemistry transport and climate models.

1 Introduction

Polar stratospheric clouds (PSCs) play an essential role in the depletion of stratospheric ozone (Solomon, 1999). Although they have been explored for more than 30 years, there are still many open questions that limit our ability to predict the formation and surface area of different PSCs and, consequently, the prediction of future polar ozone loss rates in a changing climate system. With the continued implementation of the Montreal Protocol and its amendments and adjustments, a recovery of the ozone hole and the disappearance of the Antarctic ozone hole is projected to occur by the end of the century. However, there is a large uncertainty in estimates of the rate and timing of this recovery (Eyring et al., 2013, WMO, 2014). Accurate projections of the timing of recovery are critical, as it will further reshape southern hemisphere climate and weather (Polvani et al., 2011, Gerber and Son, 2014). These projections are necessary for deciding climate change mitigation and adaptation policies.

The difficulty in making accurate predictions stems from a variety of problems of chemistry-climate models (CCMs), where one important problem is the poor representation of PSCs. CCMs used for assessments of stratospheric ozone loss (e.g., Eyring et al., 2013) often employ rather simple heterogeneous chemistry schemes. The simpler schemes are frequently based on nitric acid trihydrate (NAT), although it is known that heterogeneous chemistry on super-cooled ternary solution (STS) and on cold binary aerosol particles probably dominates polar chlorine activations (e.g., Solomon, 1999; Drdla and Müller, 2012). The models usually do not include comprehensive microphysical modules to describe the evolution of different types of PSCs over the winter. In addition, mesoscale temperature variations caused by gravity waves are crucial for the formation of PSCs under conditions close to temperature threshold conditions (e.g,. Carslaw et al., 1998, Engel et al., 2013), but are missing from the current generation of CCMs (Orr et al., 2015).

PSCs are classified according to their composition into three types. The discrimination is important as catalytic ozone destruction can be sensitive to PSC composition, and the formation of PSC types is extremely temperature sensitive. Super cooled ternary solutions (STS) form by condensation of HNO_3 and water vapour on stratospheric background sulphate aerosols. This occurs at temperatures 2-3 K below the existence temperature of solid nitric acid trihydrate (NAT) particles at T_{NAT}~195 K. The formation of NAT by homogeneous nucleation requires much lower temperatures. This is usually 3-4 K below the ice frost point T_{ice} at ~185 K, where ice particles are formed (e.g., Grooß and Peter, 2013). The formation of STS droplets is well understood (e.g., Carslaw et al., 1995), but for NAT and ice particles new formation mechanisms by heterogeneous nucleation on meteoric smoke well above T_{ice} are under discussion (Hoyle et al., 2013, Engel et al., 2013, Grooß et al., 2014). These so far new pathways for NAT and ice formation are supported by the observation of an unusually large amount of refractory submicron aerosols of most likely meteoric origin in composition measurements of cloud condensation nuclei (Weigel et al., 2014). The wide-spread detection of PSC containing NAT particles well above T_{ICE} in satellite observations in northern hemisphere winters without indication for orographic gravity waves is a distinctive indicator for a formation mechanism of NAT particles independent from pre-existing ice particles (Hoyle et al., 2013).

Atmos. Meas. Tech. Discuss., doi:10.5194/amt-2016-20, 2016
Manuscript under review for journal Atmos. Meas. Tech.
Published: 15 February 2016

Progress on the evaluation of CCMs and Chemical Transport Model (CTM) results is currently limited regarding PSC processes, as detailed long-term observations of PSCs are not available at present. For instance, solar occultation measurements of PSCs rarely discriminate the cloud type, and cannot be conducted in the polar night. However, the wintertime polar regions have been covered for several years by remote sensing satellite instruments which are not dependent on the sun as a light source, A 10 year archive (2002–2012) of measurements from the Michelson Interferometer for Passive Atmospheric Sounding (MIPAS) (Fischer et al., 2008) on-board ESA's Environment Satellite (Envisat) and ongoing measurements from the Cloud-Aerosol Lidar with Orthogonal Polarization (CALIOP) instrument from the NASA/CNES Cloud-Aerosol Lidar and Infrared Pathfinder Satellite Observations (CALIPSO) mission (Winker et al., 2009) started in May 2006, are available.

This paper introduces a new classification method of the composition of PSCs based on IR limb measurements and first applications on the MIPAS data. After the introduction, the paper will present details on instruments and data sets used in the analyses (Sec. 2), followed by a review of both formerly adopted, and new classification methods (Sec. 3). Supported by radiative transfer calculations and the MIPAS measurements themselves, all methods are combined in a new Bayesian classifier (BC) for a comprehensive PSC composition classification for MIPAS. Section 4 presents some examples of the completely processed dataset, as well as a comparison with the CALIOP instrument.

2 Instruments and datasets

2.1 MIPAS instrument on Envisat

MIPAS on board the ENVISAT satellite measured limb infrared (IR) spectra in the wavelength range from 4 to 15 µm (Fischer et al., 2008) from July 2002 to April 2012. The satellite operated on a sun synchronous orbit (inclination 98.4°) and allowed geographical coverage up to both poles due to additional poleward tilt of the primary mirror. The high spectral resolution of 0.025 cm^{-1} (HR: high-resolution mode) was changed in 2004 to 0.0625 cm^{-1} (OR: optimised-resolution mode) due to technical problems with the interferometer (Raspollini et al, 2013). Consequently, the level 1b radiance data from the measurement period July 2002 to March 2004 (Phase 1) are measured in the HR mode and from January 2005 to March 2012 (Phase 2) in the OR mode. Vertical and horizontal sampling for the nominal measurement modes are changed from Phase 1 to 2. In Phase 1 a constant 3 km grid was used up to a tangent height of 42 km. In Phase 2 this changed to a latitude dependent vertical step size of 1.5–4.5 km (starting tangent altitudes ranging from 5–70 km at the poles to 12–77 km over the equator), with steps increasing with height from 1.5 to 4.5 km. The horizontal sampling changed from 550 km to 420 km. The vertical field of view (FOV) of MIPAS has a trapezoidal form with a base width of 4 km and top width of ~2.8 km. The cross track FOV is 30 km.

2.1.1 MIPAS cloud measurements

In the following analyses we make use of the cloud detection results of the MIPcloud processor (Spang et al., 2012) Version 1.2.0, a prototype processor originally developed during an ESA study on fast cloud processor products for MIPAS-Envisat (Spang et al., 2010a, 2010b). Various detection methods are applied in the processor, like the cloud index (CI) colour ratio approach (Spang et al., 2004) with constant and variable detection threshold values, as well as variable with latitude and altitude (Spang et al., 2012, Sembhi et al., 2012). In addition, a more sophisticated retrieval approach with simplified assumptions for the radiative transfer in clouds (Hurley et al., 2011) is implemented. The retrieval copes with the difficulty of using a 3 km vertical FOV to determine a more realistic cloud top height (CTH) inside the FOV. A step-like data processing approach of up to 5 methods was chosen for the MIPclouds processor to provide a summary CTH information with the best possible detection sensitivity (Spang et al., 2012). We use this approach for the detection of the first cloud affected spectrum in an altitude scan for starting with the PSC classification.

Figure 1 shows examples of PSC spectra measured by MIPAS and classified as ice, NAT and STS. The spectral resolution is reduced to 1.2 cm^{-1} by applying a Gaussian instrument line shape with corresponding width. The resulting resolution is usually sufficient to highlight differences in the continuum like emission of the different PSC types. Aerosol and cloud particles rarely produce sharp spectral features, and the strong spectral signature of NAT at 820 cm^{-1} is an exception (Spang and Remedios, 2003, Höpfner et al., 2006a).

The MIPAS detection sensitivity for clouds and aerosol is excellent. Due to the long limb path through the tangent height layer (i.e., ~400 km for a 3 km vertical FOV at 20 km altitude) the instrument integrates all scattered and emitted radiation from cloud particles of a large volume of air spread along the line of sight. Based on radiative transfer modelling, Spang et al. (2015) estimated the detection sensitivity of an IR limb sounder with respect to the ice water content (IWC) for cirrus clouds in the lowermost stratosphere. These conditions are transferable to ice PSCs in the polar vortices. A cloud layer with 1 km horizontal extent should be detectable with IWC > 0.3 mg/m^3 (and therefore a 100 km extent with IWC > 0.003 mg/m^3), if the vertical and cross-track direction of the FOV is completely filled by the cloud. This represents an extremely high detection sensitivity, even better than most of the current tropospheric cloud products of the CALIOP lidar, where most products typically are based on a 5 km horizontal averaging (Avery et al., 2012).

An algorithm for PSC type classification was already part of the MIPclouds processor but showed various problems and spurious results in comparison with space and ground based measurements. Therefore, we developed a new more reliable classification scheme partly based on methods already applied in the MIPclouds processor and a new approach for the combination of several brightness temperature differences with these methods.

Atmos. Meas. Tech. Discuss., doi:10.5194/amt-2016-20, 2016
Manuscript under review for journal Atmos. Meas. Tech.
Published: 15 February 2016

Atmospheric Measurement Techniques
Discussions
Open Access

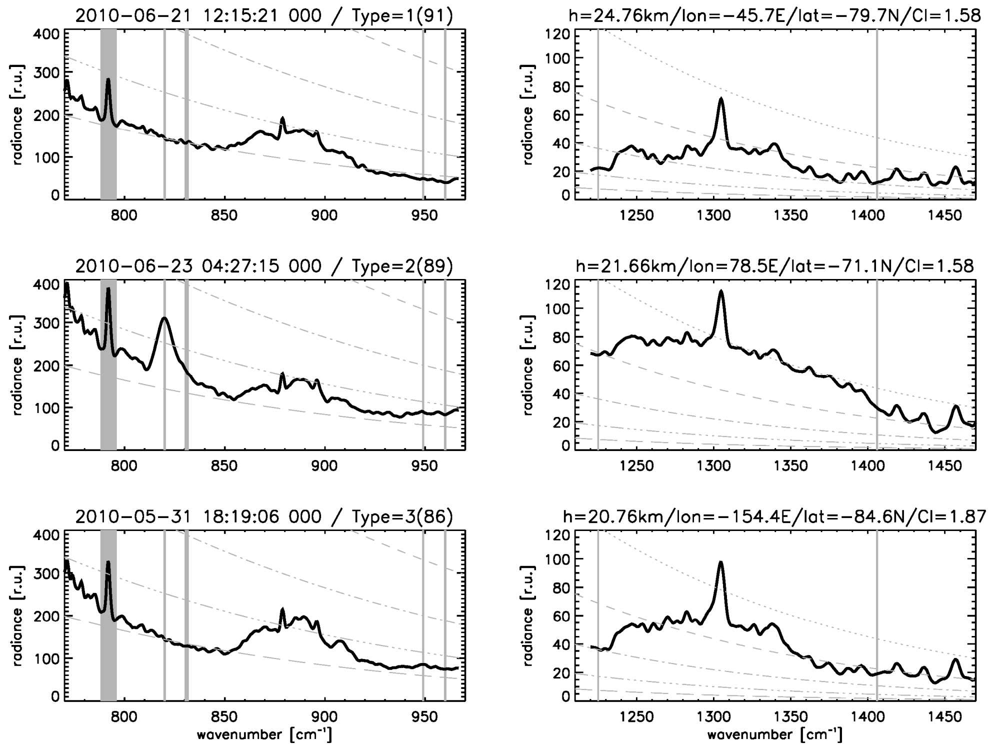

Figure 1: Examples of MIPAS radiance spectra in radiance units (1 r. u. = 10^{-9} W / (cm^2 sr cm^{-1})) in the two main wavelength regions of interest. Spectra are classified with ice (top), NAT (middle), and STS (bottom) with high confidence in classification (P_{type} = 91/89/86 %, see Sec. 3.3). Superimposed by grey bars are the selected wavelength regions for the classification scheme. The spectral resolution is degraded to ~1.2 cm^{-1} with a sampling of 0.35 cm^{-1}. Additional Planck functions for 140 to 180 K in 10 K steps are superimposed in grey dash/dotted curves.

2.2 Cloud Scenario Database

As a part of the MIPclouds study (ESA, 2008, Spang et al., 2012), a comprehensive cloud scenario database (CSDB) was compiled of modelled MIPAS radiance spectra in the presence of various cloud types and different atmospheric conditions. The database contains more than 70,000 different cloud scenarios and more than 600,000 spectra affected by PSCs (STS, NAT, and ice), cirrus and liquid water clouds (Spang et al., 2008).

An optimised list of window regions was selected for the database with a total spectral range of 137 cm^{-1}: 782-841, 940-965, 1224-1235, 1246-1250, 1404-1412, 1929-1935, 1972-1985, 2001-2006, and 2140-2146 cm^{-1}. The CSDB spectra were

Atmos. Meas. Tech. Discuss., doi:10.5194/amt-2016-20, 2016
Manuscript under review for journal Atmos. Meas. Tech.
Published: 15 February 2016

Atmospheric Measurement Techniques Discussions

generated with the Karlsruhe Optimized and Precise Radiative transfer Algorithm (KOPRA) model (Stiller, 2000), which takes single scattering into account (Höpfner, 2004). Input parameters, such as effective radius, volume density, cloud type, and composition (e.g., three possible H_2SO_4/HNO_3 compositions for STS: 02%/48%, 25%/25%, and 48%/02% with 50% H_2O) as well as cloud top and bottom height, were varied for the database. Table 1 presents a summary of the parameter space covered by the input parameters of the model runs, including the particle size distribution (PSD). Refractive indices for NAT by Biermann et al. (2000) and Höpfner et al. (2006a), for ice by Toon et al. (1994), and for STS by Biermann et al. (2000) were applied for the computation of the single scattering properties of spherical particles.

Table 1: Summary of Cloud Scenario Database parameter space

PSC type	**Volume Densities** [μm^3 cm^{-3}]	**Median Radius** [μm]
Ice	10, 50, 100	1.0, 2.0, 3.0, 4.0, 5.0, 10.0
NAT	0.1, 0.5, 1.0, 5.0, 10.0	0.5, 1.0, 2.0, 3.0, 4.0, 5.0
STS 02/48 (*)	0.1, 0.5, 1.0, 5.0, 10.0	0.1, 0.5, 1.0
STS 25/25 (*)	0.1, 0.5, 1.0, 5.0, 10.0	0.1, 0.5, 1.0
STS 48/02 (*)	0.1, 0.5, 1.0, 5.0, 10.0	0.1, 0.5, 1.0
Cloud top height [km]	**Cloud vertical extent [km]**	**Cloud minimum bottom height [km]**
28.5 - 12.5 with 1km spacing	0.5, 1, 2, 4, 8	12
Modeled tangent heights:	30 km down to 12 km with 1 km spacing	

(*): Weight percentages of H_2SO and HNO_3 are noted (e.g.,, 02/48 means 2 wgt% H_2SO_4 and 48 wgt% HNO_3)

The radiative transfer calculations assume a homogeneous cloud layer, filling the tangent height layer with PSC particles. This simplified 1D geometry is not generally applicable for a limb-scanning instrument. Under realistic atmospheric conditions, broken cloud fragments of various scales in front or behind the tangent point can be expected. Although these 2D effects are not explicitly modelled in the database, various cloudy path lengths are already included. The scenarios of the simulated spectra of the CSDB take into account tangent heights well below the cloud base for various cloud thickness (see **Table 1**). This results in quite representative and variable lengths of cloud segments along the line of sight. Spang et al. (2012) showed that detection sensitivity and optically thickness in the limb strongly relate to the integrated volume density path (VDP) or the integrated area density path (ADP) along the line of sight. Subject to the particle median radius *r*, this is ADP for cloud types with larger particles ($r > 5$ µm, typically ice clouds) and VDP for small median radii ($r < 5$ µm, like STS, NAT, and sulphate aerosols). The variable lengths of cloud segments in the CSDB results in a broad variability in ADP and VDP, which would occur in the real atmosphere for broken cloud segments along the line of sight. Finally, note the cloud index correlates well with VDP and ADP, depending on the cloud type. Spang et al. (2012) showed that CI is a useful proxy for the optical thickness of the cloud and that it is possible to estimate VDP or ADP from the CI measurements depending on the particle type.

Atmos. Meas. Tech. Discuss., doi:10.5194/amt-2016-20, 2016
Manuscript under review for journal Atmos. Meas. Tech.
Published: 15 February 2016

2.3 CALIOP instrument on CALIPSO

The CALIOP instrument is a dual wavelength polarization sensitive lidar that provides high vertical resolution profiles of backscatter coefficients at 532 and 1064 nm (Winker et al., 2009). The CALIOP instrument is a part of the CALIPSO nadir viewing sun-synchronous satellite system inclined at 98° at an altitude of 705 km. The orbit geometry facilitates measurements up to latitudes of 82° N/S, compared with of 87°S to 89°N for MIPAS.

In this study, we used lidar level 2 Polar Stratospheric Cloud Mask data downloaded from http://eosweb.larc.nasa.gov/. The CALIOP product comprises cloud and aerosol backscatter coefficient profiles at 5 km horizontal and 180 m vertical sampling size. The PSC detection and classification is so far limited to observations at night because higher levels of background light during daytime significantly reduce the signal-to-noise ratio. A successive horizontal averaging of 5, 15, 45 or 135 km is applied to the data to improve the signal-to-noise ratio for the detection of optically thin clouds (typically necessary for STS and NAT clouds) (Pitts et al., 2009).

The second-generation CALIPSO PSC algorithm (Pitts et al., 2009) detects clouds using both the CALIOP 532-nm scattering ratio (the ratio of total to molecular backscatter) and the 532-nm perpendicular backscatter coefficient. The algorithm also includes a scheme for classifying PSCs by composition based on the measured CALIOP aerosol depolarization ratio and the inverse scattering ratio. Pitts et al. (2009) defined four PSC composition classes for the CALPSO measurements: STS, water ice, and two classes (Mix 1 and Mix 2) of liquid/NAT mixtures. Mix 1 denotes mixtures with very low NAT number densities (from about 3×10^{-4} cm^{-3} – the inferred CALIOP NAT sensitivity threshold – to 1×10^{-3} cm^{-3}), while Mix 2 denotes mixtures with higher (> 10^{-3} cm^{-3}) NAT number densities.

The STS class may also include low number densities of NAT particles whose optical signature is masked by the more numerous liquid droplets of STS at cold temperatures (Pitts et al., 2013). High number densities of NAT particles, that are not masked by liquids, lying within the rest of the Mix 2 domain and are described with Mix 2 enhanced (Mix 2-enh). Finally, the data show for intense mountain-wave induced PSCs a subset of CALIPSO ice PSCs in the parameter space. Through their distinct optical signature in the scattering ratio and lidar colour ratio (the ratio of 1064-nm to 532-nm aerosol backscatter coefficients) this CALIPSO class is easily to separate from usual ice observations and is described with wave-ice. Consistent with mountain wave PSCs this type is characterised by a high ice particle number density (100% ice activation from the background aerosol) but relatively small particles (1–1.5 µm radius, e.g., Pitts et al., 2009).

2.4 AIRS instrument

In this study, we use radiance measurements of the Atmospheric Infrared Sounder (AIRS) (Aumann et al., 2003; Chahine et al., 2006) to detect gravity waves in the polar lower stratosphere. AIRS is one of six instruments aboard the National Aeronautics and Space Administration's (NASA's) Aqua satellite. Aqua was launched in May 2002 and is the first satellite in NASA's `A-Train' constellation of satellites. Aqua operates in a nearly polar, sun-synchronous orbit (705 km altitude, 100 min period, 100° inclination). AIRS measures about 2.9 million infrared nadir and sub-limb spectra per day. Spectral measurements

cover the wavelength range from 3.74 to 15.4 µm in three bands. Noise varies between 0.07 and 0.7 K at 250 K scene temperature. AIRS performs across-track scans, covering 1780 km distance on the ground and consisting of 90 footprints each. The footprint size of AIRS varies between 14 x 14 km^2 at nadir and 42 x 21 km^2 at the scan extremes. Due to its measurement geometry AIRS is capable of detecting gravity waves with short horizontal and long vertical wavelengths.
Here, gravity wave information is provided in terms of brightness temperature variances of the AIRS channels covering the 15 µm waveband of CO_2, being most sensitive to atmospheric temperatures at about 15-40 km altitude, with a maximum in the weighting function around 20-30 km. Spectral averaging and corrections to reduce noise and the de-trending procedure for removing background signals due to large-scale temperature gradients or planetary waves follow the approach of Hoffmann et al. (2013, 2014).

3 PSC type classification methods for IR limb sounding

All classification methods presented below are based on characteristic spectral differences in the absorption and scattering efficiency of the three types of PSCs (STS, NAT, and ice) known to occur in the polar stratosphere (Peter and Grooß, 2013). At this point we should clarify that in the following the term 'PSC type' and 'mixed-type' is not related to the lidar-based classification of PSC observations of Type 1a, 1b, and Type 2 frequently used in the literature (e.g., Achtert and Tesche, 2014, and references therein). Here, the word type represents the three different types of particle composition, namely STS, NAT, and ice, which can affect and may dominate and the spectral characteristics of a single measured infrared spectrum. The refractive indices of the particle type together with its size distribution are the key input parameters for the computation of the optical properties by the Mie-Theorie (Mie, 1908), i.e., absorption and scattering efficiency and the scattering phase function. The wavelength dependence of real (n_r) and imaginary (n_i) part of the refractive index (r_i) for ice, NAT and STS is presented in **Figure 2**. Where n_i is responsible for the absorption and n_r for the scattering characteristic of the particle type. Obviously, gradients and value of r_i can be very different depending on the part of the spectral region and the particle type. The r_i's based on laboratory data are used in the radiative transfer calculations for the CSDB (**Sec. 2.2)**. All wavelength regions of the final multi-wavelength classification method are superimposed in **Figure 2**.

3.1 Two-colour-ratio method

Originally, Spang and Remedios (2003) introduced the two-colour-ratio method (2CR) for the classification of PSC spectra based on Cryogenic Infrared Spectrometers and Telescopes for the Atmosphere (CRISTA) observations (Offermann et al., 1999, Grossmann et al., 2002). Höpfner et al. (2006a) further developed the method and compared the results with the CALIPSO PSC classification scheme (Höpfner et al., 2007). The 2CR method includes one colour ratio sensitive to the optical thickness and extinction of the cloud ($CR_1 = I_{11}(788.2\text{-}796.2\ \mathrm{cm^{-1}}) / I_{12}(832.0\text{-}834.4\ \mathrm{cm^{-1}})$), which was originally introduced as the cloud index (CI) for the detection of cloudy and non-cloudy spectra in the CRISTA and MIPAS radiance datasets (e.g., Spang et al., 2005). A second colour ratio is sensitive to a spectral feature attributed to the emissions of small NAT particles

Atmos. Meas. Tech. Discuss., doi:10.5194/amt-2016-20, 2016
Manuscript under review for journal Atmos. Meas. Tech.
Published: 15 February 2016

Atmospheric Measurement Techniques Discussions
Open Access

($CR_2 = I_{21}\,(819.0\text{-}821.0\ \mathrm{cm}^{-1}) / I_{22}\,(788.2\text{-}796.2\ \mathrm{cm}^{-1})$) (Höpfner et al., 2006a), referred to in the following as the NAT index (NI). The method traces back to a study of the first observations of a NAT spectral signature at 820 cm^{-1} from space during the CRISTA-2 mission (Spang and Remedios, 2003). There is also a small but strong feature at this wave number range (**Figure 2**), caused by the ν_2 band emissions of NO_3^- (Höpfner et al., 2002). In former laboratory measurements of NAT refractive indices the feature was not pronounced enough to reproduce the atmospheric infrared limb observations of the signature. But in a reanalysis of the Biermann et al. (2000) NAT film measurements in conjunction with radiative transfer model calculation, Höpfner et al. (2006a) showed the unambiguous assignment that NAT particles with $r < 3\ \mu m$ produce the spectral signature in the measured spectra.

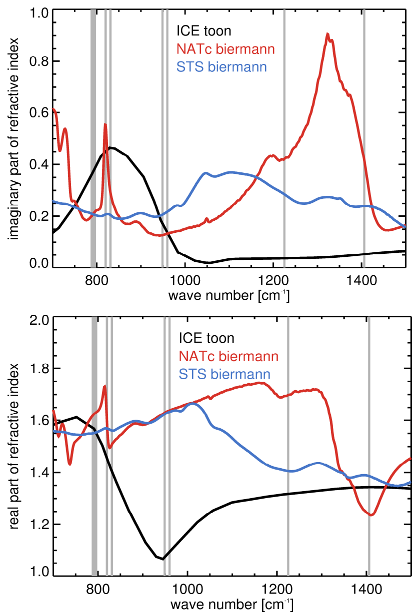

Figure 2: Refractive indices (imaginary part at top and real part at lower panel) of ice clouds (Toon et al. 1994), coated NAT (Biermann et al., 2000, Höpfner et al., 2006a), and STS with weight percentages of composition of 17 wgt% HNO_3 and 25 wgt% H_2SO_4 (Biermann et al., 2000). Superimposed in grey are the wavelength regions applied in the classification scheme.

Figure 3 presents examples of the probability density distribution function (PDF) of CI versus NI for MIPAS in the months May, June, August and September for the southern hemisphere winter 2007. In the PDFs additional separating lines (dash-dotted) are superimposed for regions in the parameter space where specific PSC types are dominating the distribution. The separating lines are retrieved from radiative transfer calculations for varying particle size distributions and composition

Atmospheric Measurement Techniques Discussions

(Höpfner et al., 2006a). They split the parameter space into one region above the curve, where events are definitely attributed to NAT with a particle median radius r < 3 µm. Larger particles of NAT and ice appear in the parameter space below the curve and are difficult to separate from STS, which are usually found in the area below the curve for CI>1.3. Finally, spectra for ice are observed below the curve but for CI<1.3. Typical water vapour mixing ratios (2-6 ppm) and temperatures below 190 K in the polar winter stratosphere suggest the formation of ice clouds with volume densities of optically thick conditions in the limb direction. For example, a homogeneous ice water content of 1 ppmv over the entire domain of the tangent height layer will produce an extinction of around 3 x 10^{-2} km^{-1} which is equivalent to optically thick conditions in the limb direction (Spang et al., 2008) and values of CI < ~1.2 (see also **Figure 1**). The effective cloudy limb path is a crucial parameter for the observed optical thickness. The CI method is mainly sensitive to the limb integrated volume density or area density path along the line of sight (Spang et al., 2012, 2015), and therefore small broken clouds fragments with high optical thickness along the line of sight can be detected with a moderate CI value. This is also the case for an optical thinner but horizontally extended cloud layers.

For the CSDB we used an extended parameter space (e.g., smaller volume densities for ice and larger for NAT and STS, see Sec. 2.2). This is because optically thinner ice clouds can form in the polar stratosphere or at least can remain after the sedimentation of larger particles. In addition, the potentially available HNO_3 allows the formation of relatively high volume densities with CI<1.3 NAT and STS clouds. Finally, the CSDB shows that the region attributed to ice can also include large NAT particles (r > 3 µm) or STS with large volume densities and corresponding large optical thickness. On the other hand, the STS_{mix} region can include optically thin ice clouds. The formation of relatively large volume densities for NAT and STS is conceivable for conditions with high HNO_3 gas phase values like for early winter with no de-nitrification or late winter in regions where re-nitrification takes place.

Although these uncertainties restricts the classification capability, the 2CR method turned out to be an extremely valuable tool for the analysis of PSC type distribution over Antarctic and Arctic winter periods (Spang et al, 2005a, Spang et al., 2005b, Höpfner et al. 2006b, Eckermann et al., 2009). The application of this method to MIPAS allowed for the first time the detection of an Antarctic stratospheric belt of NAT PSCs caused by mountain waves (Höpfner et al., 2006b). In addition, the method showed a reasonable agreement with ground and space borne lidar measurements of PSC composition (Höpfner et al., 2009).

The PDFs in **Figure 3** show a characteristic and expected development over the winter. In early winter (May), STS or STS_{mix} clouds dominate the PDF, which is in line with temperatures at this time of the year. Temperatures in May are usually not cold enough to form ice (T_{ICE} ~187 K). Consequently, only little indications for NAT particles are found, whereby in June NAT events become more prominent. Temperature perturbations induced by mountain waves over the Antarctic Peninsula may cause a NAT-cloud seeding, which can affect the entire outer vortex region (Höpfner et al., 2006b, Eckermann et al., 2009). In August, temperatures are cold enough to form ice and NAT in large areas of the polar vortex causing two maxima in the distribution. In September the synoptic temperatures rise significantly above the T_{ice} threshold, where also NAT is more difficult to form and the distribution show less pronounced maxima. The method still suggests a strong probability for NAT clouds, which is disputable under the assumption that NAT is only formed for $T<T_{ice}$. However, the observations are in line

Atmos. Meas. Tech. Discuss., doi:10.5194/amt-2016-20, 2016
Manuscript under review for journal Atmos. Meas. Tech.
Published: 15 February 2016

with recent results of Engel et al. (2013) and Hoyle et al. (2013) showing the evidence for a process of heterogeneous NAT nucleation at T>T_{ice} for Arctic PSC events.

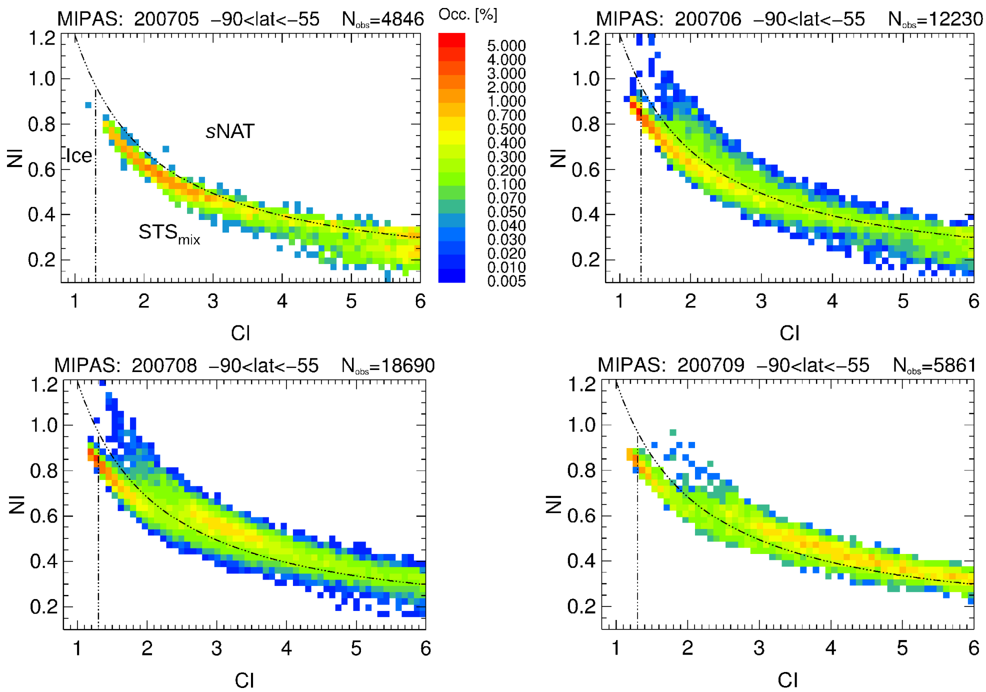

Figure 3: Probability density functions for cloud index (CI) versus NAT index (NI) for southern hemisphere 2007 winter months May, June, August and September (200705-200709) derived from MIPAS measurements in percentage of occurrence with respect to the number of observations (N_{obs}). Superimposed are the cloud type regions and separating lines related to small NAT (sNAT), ice and STS_{mix} particles from Höpfner et al., (2006a).

3.2 Brightness temperature difference methods

The 2CR method introduced above includes three different wavelength regions within the 790-833 cm^{-1} range and does not make use of the rather broad spectral ranges covered by MIPAS. **Figure 2** indicates further differences in refractive indices of different PSC types. Therefore, we investigated the benefit of adding further spectral regions in detail.

Atmos. Meas. Tech. Discuss., doi:10.5194/amt-2016-20, 2016
Manuscript under review for journal Atmos. Meas. Tech.
Published: 15 February 2016

Atmospheric Measurement Techniques Discussions
Open Access

3.2.1 Combined CR-BTD classification

Analyses of brightness temperature differences (BTD) are frequently applied to nadir sounders for the differentiation of tropospheric aerosol, liquid and ice water clouds (e.g., Li et al., 2003, Clarisse et al., 2013). Usually the methods are using the characteristic strong gradient in absorption and scattering efficiency between ~800 cm^{-1} and ~950 cm^{-1} (see also **Figure 2**) for the differentiation of ice from other aerosol types. This characteristic gradient has been exploited in several recent studies using MIPAS observations (Spang et al., 2012, Grainger et al., 2013, Griessbach et al., 2014).

A first attempt to apply this wavelength dependence to limb measurements was realised in an ESA study for the development of a fast cloud parameter processor for MIPAS (Spang et al. 2010, 2012). **Figure 4** shows a CR-BTD combination with CI versus $BTD_{833\text{-}849}$ = BT(833 cm^{-1}) – BT(949 cm^{-1}) of the modelled CSDB spectra. A significant separation is observable between ice and STS. However, NAT and STS have a relative similar distribution. Large NAT particle lose their characteristic wavelength dependence in the radiance emissions and an explicit differentiation becomes difficult in a large overlap region for NAT and STS.

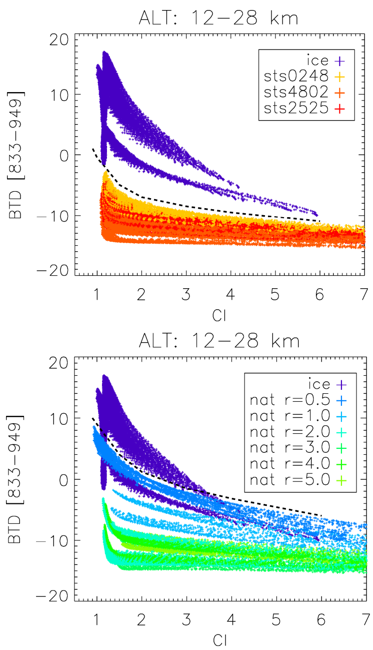

Figure 4: Modelled cloud index (CI) versus brightness temperature difference between 833 cm^{-1} and 949 cm^{-1} for all PSC scenarios of the CSDB. Top: for ice compared to three STS compositions (colour coded, see also **Table 1**), and bottom: ice compared to NAT (colour coded NAT radii). Superimposed dashed lines separate ice events from the corresponding second PSC composition in the figure, STS (top) and NAT (bottom), respectively.

Atmos. Meas. Tech. Discuss., doi:10.5194/amt-2016-20, 2016
Manuscript under review for journal Atmos. Meas. Tech.
Published: 15 February 2016

Atmospheric Measurement Techniques Discussions
Open Access

Examples of two PDFs of the MIPAS CR-BTD distribution are presented **Figure 5** for NH winter 2010/11, a record winter for Arctic ozone destruction (e.g., Manney et al., 2011). During this outstanding NH winter, CALIOP observed unusual high occurrence rates for ice clouds. Typically, for most of the NH winter distributions (see examples) and for SH early winters (May, not shown) there is no activity observed in the area attributed to ice and only occasionally in the ice-NAT area. We take into account that the spectra influenced by cloud emission show CI smaller than 5-6 depending on altitude (Spang et al., 2005a, Höpfner et al. 2006a) and typical detection thresholds are usually even a bit smaller (4.0-4.5). Starting in February 2011 (**Figure *5***, bottom) for a phase of 4-6 weeks, synoptic cold temperatures in the range well below T_{NAT} and close to T_{ice} are observed (Arnone et al. 2012, Manney et al., 2011). This fits to the MIPAS observations for February with a large number of cloud events with significant ice signatures typical for SH mid-winter conditions.

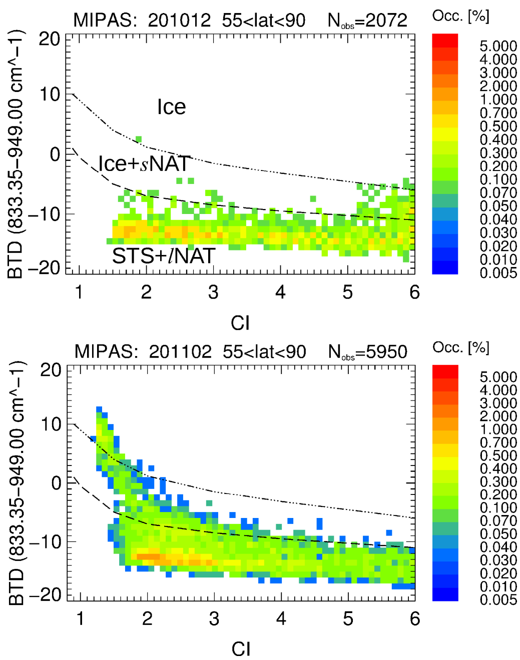

Figure 5: MIPAS two-dimensional PDF distribution of cloud index (CI) versus $BTD_{833\text{-}949}$ for the Arctic Dec 2010 (top) and Feb 2011 (bottom) measurement periods in the altitude range 16 to 30 km. Superimposed separation functions (dashed-dotted and dashed lines) are retrieved from the CSDB in **Figure 4** and are highlighted with Ice (top), Ice+sNAT (middle) for the overlap region of ice with small NAT particles, and for the overlap of STS with large NAT (*l*NAT) particles (bottom region).

3.2.2 2D-BTD classification methods

To further improve the PSC classification, tests with various two-dimensional BTD PDFs and scatter diagrams of the MIPAS measurements and the CSDB were performed with major focus on the atmospheric window regions so far not considered in the two classification methods discussed above. Randomly chosen mean radiance pairs, spectrally integrated over 1 cm^{-1} intervals, were considered in this test. The main intention was to find some additional information to better discriminate STS and NAT clouds. This is non-trivial because the optical properties become very similar between both types if the NAT particles have a large radius, like the so-called NAT rocks (Fahey et al., 2001).

Finally, two additional wavelength regions at 1225 cm^{-1} and 1406 cm^{-1} were found to add most complementary information for the classification of PSC. The 1406 cm^{-1} radiances add some radius sensitivity in the NAT/STS differentiation in the $BTD_{820-831}$ versus $BTD_{1406-960}$ distribution. The first BTD has its main contrast with respect to enhanced emissions at 820 cm^{-1} caused by small NAT particles (cf. **Figure 6**), but also the ice distribution shows some radius sensitivity for $BTD_{820-831}$. STS clouds tend to appear in regions separated from NAT and highlighted by the dashed polygon. Only a part of the large radius NAT clouds (3 and 5 µm) are able to overlap the area attributed to STS. $BTD_{1406-960}$ seems to improve the separation of the medium NAT particles (1 - 3 µm) from STS. In addition, it is sensitive to the optical thickness of the cloud. The two BTDs tend to shrink close to zero for optically thicker conditions (see colour coded volume density path).

Figure 7 presents PDF distributions of MIPAS measurements for the same BTDs shown in **Figure 6** for NH and SH winter months. Over the SH winter 2010 the distributions indicate that STS particles dominate the early winter (May). For June the maximum shifts to the left shoulder of the STS_{mix} (MIX) area, most likely due to the formation of ice, while in July the more pronounced NAT formation results in a bi-modal distribution. The bi-modality stays until late winter (September) and is typical for all SH late winter conditions like the other MIPAS SH winter observations are suggesting. Due to the much shorter PSC season in the NH and consequently less frequent formation of ice, the PDF looks very different. The small ice (sICE) and upper mixed-type (MIX) events are only observed in a few years of the monthly PDFs for the NH. However, 3 out of 10 very cold winters in the MIPAS measurement period show an extension of the distribution into the sICE area. Finally, the incorporation of the wavenumber region at 1225 cm^{-1} improved the discrimination of ice from NAT and STS using a $BTD_{831-1225}$ versus $BTD_{960-1225}$ scatter diagram of the CSDB distribution (not shown).

Figure 8 shows examples for the MIPAS 2010/11 measurements, again for NH (January 2010 and December 2011) and four for SH conditions (May 2010, and August 2009, 2010, and 2011). The CSDB showed for the new BTD combination a distinctive sensitivity for a better ice discrimination and some radius sensitivity. Only ice particles of large radius (10 µm) and low ADP (Sec. 2.1.1) can appear close and below the borderline to the region attributed to MIX (STS and NAT). All other modelled ice spectra appear below the borderline and ice clouds with small radii but high ADP (high extinction/optical thickness) cause the elongation in direction to the right top corner of the distribution. Obviously, the ice microphysical parameters seem to change for different Antarctic August conditions (**Figure 8**).

Atmos. Meas. Tech. Discuss., doi:10.5194/amt-2016-20, 2016
Manuscript under review for journal Atmos. Meas. Tech.
Published: 15 February 2016

Atmospheric Measurement Techniques
Open Access
Discussions

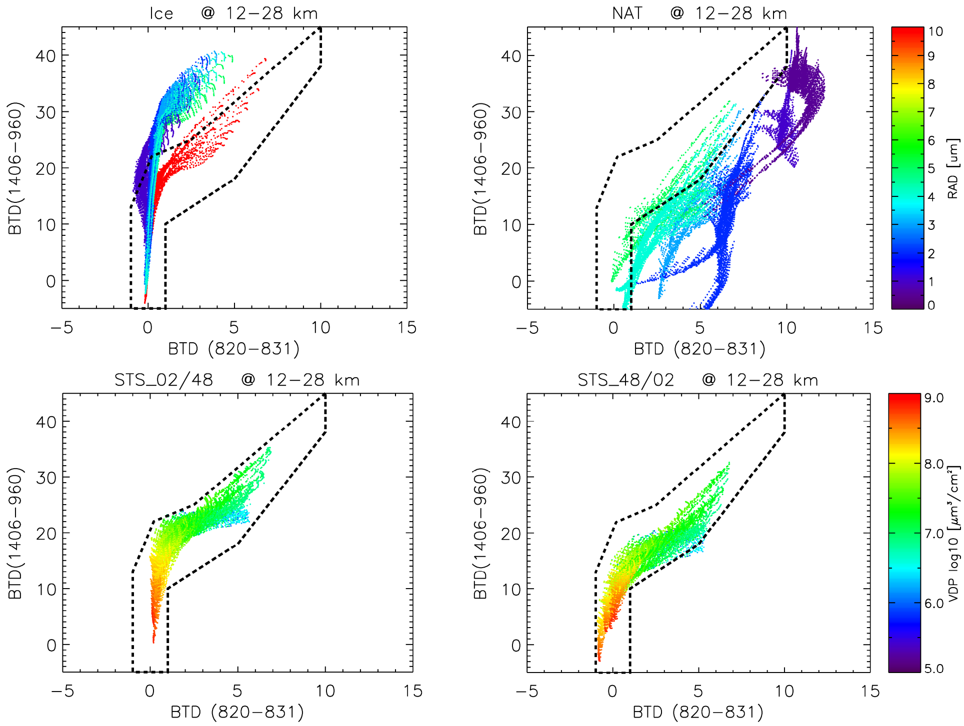

Figure 6: Scatter diagrams of BTD$_{820-831}$ versus BTD$_{1406-960}$ distribution for the CSDB spectra of Ice (top, left) and NAT (top, right) with colour coded radius dependence and two STS compositions (bottom) with colour coded volume density path (VDP) dependence. The axes ranges are restricted to the BTD ranges typically observed for MIPAS (see next figure). Only data with CI<6 are presented. The superimposed polygon (dashed line) marks the area where spectra of modelled STS composition occur in the full set of the CSDB spectra.

Atmos. Meas. Tech. Discuss., doi:10.5194/amt-2016-20, 2016
Manuscript under review for journal Atmos. Meas. Tech.
Published: 15 February 2016

Atmospheric Measurement Techniques
Discussions

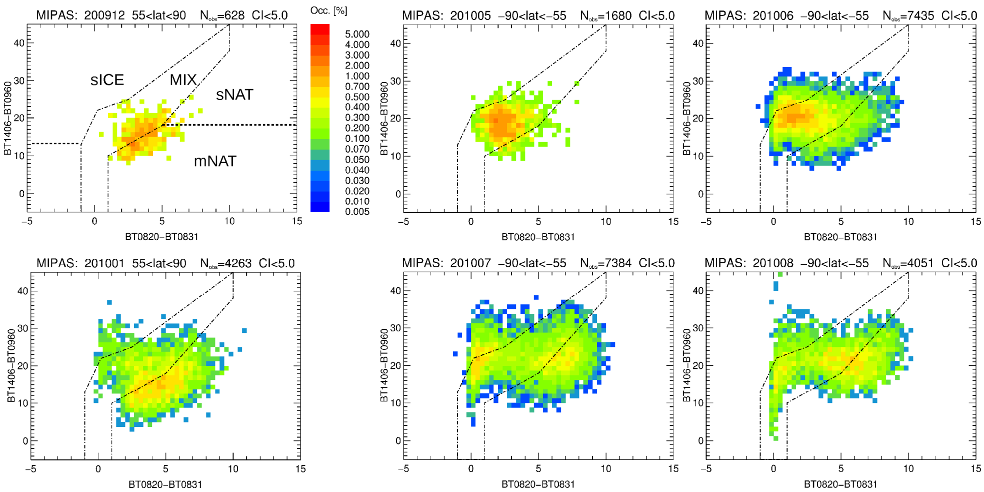

Figure 7: Monthly PDFs of $BTD_{820\text{-}831}$ versus $BTD_{1406\text{-}960}$ from MIPAS for NH Dec 2009 and Jan 2010 (left column) and SH May 2010 to Aug 2010 (middle and right column) in the altitude range 18-30 km. The colour code represents the relative occurrence in percent with respect to the total number of cloudy spectra (N_{obs}) with CI<5 for each individual spectrum. The dashed-dotted polygon highlights the region of STS occurrence. Because ice and large NAT may occur in this area as well it is indicated as MIX in the first diagram. The two horizontal lines (dashed) in this diagram create three additional areas where small ice (sICE), small NAT (sNAT) and medium size NAT particle (mNAT) dominate the distribution.

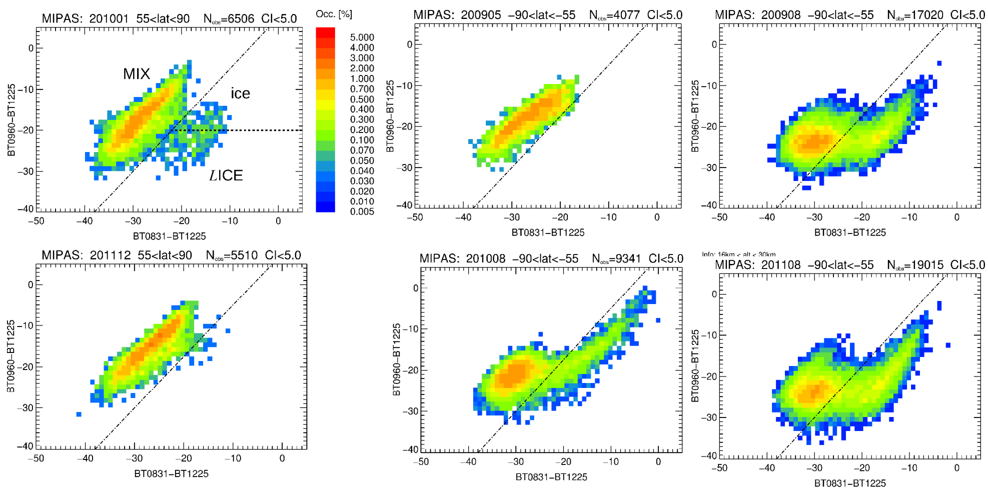

Figure 8: Monthly PDFs of $BTD_{831\text{-}1225}$ versus $BTD_{960\text{-}1225}$ are presented for NH and SH conditions north and south of 55° N/S, respectively. NH January 2010, December 2011 (left column), SH May 2009, August 2009, 2010, and 2011 (middle and right column) for all cloudy observations (CI<5) in the altitude range 16-30 km. Areas for PSC classification are highlighted by

dashed lines in the first figure (top left), where 'ice' and '*L*ICE' highlights the regions in the PDF dominated by small and large particles in the CSDB information, respectively.

3.3 Bayes classification approach

The BTD and CR combinations presented above clearly provide additional information on microphysical parameters (e.g., radius, ADP/VDP) as well as on the specific cloud type. However, discrimination with borderlines in 2D PDF distribution, as presented earlier, is often difficult because a reliable classification of events close to the threshold curves is not possible. In the following, we apply a simple probabilistic classifier based on applying Bayes' theorem with strong (naive) independence assumptions to the four BTD and CR methods described in Sec. 3.1 and Sec. 3.2. This method combines the information content of the individual classification methods (classifier) into a single estimate of the most probable PSC type dominating the measured IR spectrum, in the following referred to as Bayesian classifier (BC).

The four individual classifiers include in total 13 different classification areas, as presented in **Figure 3, Figure 5, Figure 7,** and **Figure 8**. For each of the 13 areas a probability of classification for ice, NAT, and STS $p_{i,j}$ is presented in the matrix of Table 2, where the indices $i=1,\ldots,13$ and $j=1,2,3$ refer to the classification area and cloud type, respectively. In an area in the parameter space where the modelled spectra of the CSDB suggest that only one PSC particle type occurs (little or no overlap with other types) we attributed a large probability for the specific type and only small probabilities for the other two types (e.g., ice region in **Figure 5** and acronym ICE_{CI} in Tab. 2). For areas with significant overlap, the probabilities are defined of similar size (equal probabilities of all n = 3 cloud types would result in $p_{i,j}$ = 33%). A cloudy spectrum appears in one area of the classification diagrams of the four classifier ($m=4$). The $index(k)$ (Table 2) with $k=1\ldots m$ will select always only one area per classifier (in total 4 out of 13), and represents exactly where the spectrum appears in the parameter space. Finally, we define a normalised product probability for each potential cloud type:

$$P_j = \prod_{k=1}^{m} p_{index(k),j} \quad / \quad \sum_{j=1}^{n} \left(\prod_{k=1}^{m} p_{index(k),j} \right)$$

This approach attributes to each cloud spectrum a probability for each of the three PSC types. The maximum of the normalised probability is indicating the most likely PSC type. For a more distinctive classification approach we introduced a threshold of P_j > 50% for a significant confidence that PSC type j is dominating the measured cloud spectrum. In addition, if two types have a probability between 40% and 50% this may give indication for a mixed-type cloud. This circumstance appears nearly exclusively in the data analysis for the combination NAT with STS (this mixture is named NAT_STS in the following), which most likely occur in the analysis due to the difficulties to differentiate large NAT from STS particle clouds in the MIPAS measurements. It is also reasonable that mixed-type clouds or 'sandwich' structures of both types (Shibata et al., 1997) in the FOV of the instrument generate this kind of events. Ground-based (e.g., Achtert and Tesche, 2014) and spaceborne (e.g., Pitts et al., 2011) lidar measurements with better vertical resolution than MIPAS frequently observe layered structures of different PSC types. **Table 2** summarises the $p_{i,j}$ values for all 13-classification areas of the current version (V1.2.8) of the classifier.

Note that the probabilities $p_{i,j}$ were chosen empirically. The correlation diagrams of the modelled CSDB spectra provide guidance for a realistic parameter choice.

Figure 9 shows the PDF of the normalised PSC type probabilities for all cloudy spectra in the altitude range 12 to 30 km for SH June 2009. The PDFs for ice, NAT and STS illustrate the well-defined separation of ice and non-ice events by the large count numbers for P_{ice} > 85%, even higher for P_{ice} < 5%, and very low values between the two extremes. For STS and NAT a significant number of the cloud observations show P-values between 20-50% indicating some difficulties to separate both types from each other. However, both types show also a significant number of spectra with large P-values (P_i > 65%) and suggests a robust separation by the new classification approach in the MIPAS measurements.

Table 2: Predefined PSC type probability matrix for the Bayesian classifier (V1.2.8)

index	**Classifier**	$\mathbf{p_{ICE}}$ **[%]**	$\mathbf{p_{NAT}}$ **[%]**	$\mathbf{p_{STS}}$ **[%]**	**Acronym Area (*)**
1	CI-NI (2CR)	10	60	30	$sNAT3_{H06}$
2		20	25	55	STS_*l*NAT_{H06}
3		50	20	30	ICE_STS_{H06}
4	CI-BTD	70	20	10	ICE_{ci}
5		60	30	20	ICE_{ci}_sNAT1
6		10	40	50	STS_{ci}_*l*NAT2
7	$BTD_{820\text{-}831}$	60	10	30	sICE5
8	versus $BTD_{1406\text{-}960}$	30	30	40	*l*ICE5_STS_*l*NAT3
9		10	50	40	mNAT
10		10	60	30	sNAT2
11	$BTD_{831\text{-}1225}$	60	30	10	ICE
12	versus $BTD_{960\text{-}1225}$	50	30	20	*l*ICE_sNAT
13		10	40	50	STS_*l*NAT

(*): Indices of 'H06' indicates separations line based on Höpfner et al. (2006a).
Letters *l*, m and s indicates large, medium and small sized particles, respectively.
The numbers present a rough guide to the thresholds of median radius R_{med} for the term small/large and base on the input parameter of CSDB particles size distributions of Table 1.

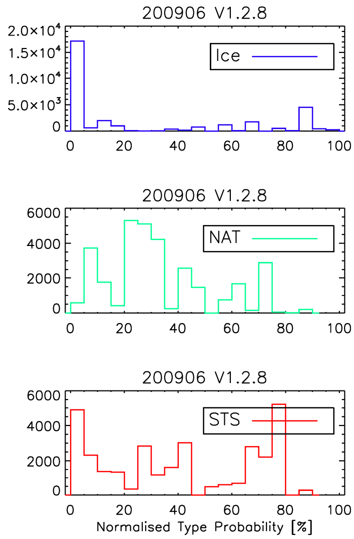

Figure 9: Event counts of the normalised probabilities P_j for ice, NAT and STS_{mix} of the Bayesian classifier for SH June 2009 cloudy spectra above 12 km altitude.

3.4 Sensitivity test of the probability matrix

We applied a Monte Carlo (MC) approach to infer the sensitivity of the classification results with respect to changes in the predefined probability matrix $p_{i,j}$ in Table 2. Gaussian perturbations with a standard deviation of 5 percentage points were applied to the original $p_{i,j}$-values. The classification was repeated 2000 times for the same input dataset of real MIPAS spectra with the perturbed probability matrix. In the example for the SH in June 2011 shown in **Figure 10** nearly 18000 PSC spectra are analysed. We selected June of the MC test for two reasons. Firstly, June is the month when usually all three PSC types exist in the SH (Pitts et al. 2009, Di Liberto et al., 2014). Secondly, in the SH during June the appearance of each cloud type is characterised by a step-like process, whereby first STS, then NAT, and finally ice PSC form. This helps to minimise uncertainties caused by patchy distributions of mixed-type clouds in mid and late winter. However, the results for other month and years are similar.

The original result of the classification approach (undisturbed probability matrix) shown in Figure 10 suggests a rather balanced occurrence of the three PSC types (25-30 %) and only a small amount of the NAT_STS mixed-type class (~6%). Additionally 5% of the analysed spectra are characterised as 'unknown', indicating that the product probabilities for ice, NAT, and STS are all smaller 40% for each class. The mean of the MC results shows a similar result for the three main classes and the unknown class, which give confidence that the selected probability matrix provides a robust classification. The definition of the probability matrix of version 1.2.8 (Table 2) has a higher tendency to select the mixed-type STS_NAT compared to the results

Atmos. Meas. Tech. Discuss., doi:10.5194/amt-2016-20, 2016
Manuscript under review for journal Atmos. Meas. Tech.
Published: 15 February 2016

suggested by the MC approach. However, the final choice of $p_{i,j}$ follows the intention of a more conservative classification approach that accounts for possible uncertainties of the differentiation between NAT and STS.

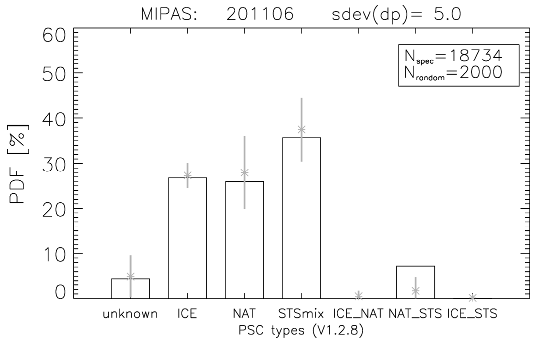

Figure 10: Probability distribution of the Bayesian classifier applied to the MIPAS spectra in the SH polar region in June 2011. Superimposed in grey are the mean value (stars) and standard deviation (error bars) of a Monte Carlo simulation varying the PSC type probability matrix (see text for details). The analysis considers only spectra at tangent heights between 16 and 28 km and up to 6 km below the CTH.

3.5 Comparison of 2CR and Bayesian Classifier

Various studies in the scientific literature applied the 2CR method for PSC classification in IR limb measurements (e.g., Spang et al., 2003, 2005, Höpfner et al. 2006b, 2009, Eckermann et al., 2009, Lambert et al., 2012, Arnone et al., 2012). Its main strength is the detection of clouds where the radiances are dominated by NAT particles with radii smaller than 3 µm (Höpfner et al., 2006a). However, Spang et al. (2012) already showed that ice particles can overlap the STS region, and vice versa, STS with large VDP may overlap the region attributed to ice (**Figure 3**).

Figure 11 presents a comparison of 2CR with our new combined Bayesian classifier for the three cloud types (ice, NAT, STS). MIPAS spectra are analysed on a monthly basis between 2007 and 2011 for the NH and SH potential PSC seasons (Nov-Mar for the NH and May-Oct for the SH, SH PSC periods are highlighted by the grey shaded sectors). Obviously, for months with strong ice formation potential (for SH the July-Sep period) the ice detection is significantly increased in the Bayes approach. In some years an enhancement even up to 30% can be observed and sums up to total amount for ice to up to 50% of all classified spectra (August 2011). The incorporation of additional wavelength regions sensitive to ice emissions seems to improve substantially the capability to classify ice spectra. Furthermore, also the partitioning between STS and NAT changes with the new approach. This becomes obvious for the NH PSC occurrences, where typically ice plays only a minor role in total abundance of PSCs due to the significantly warmer vortex temperatures. Here, the Bayesian classifier identifies more STS in contrast to NAT, but for specific winter conditions (e.g., 2009/10) this tendency is reversed. Overall, the changes are significantly smaller than for the ice class.

The general large abundance of the ice class compared to NAT and STS for both methods in the SH winters might be related to sampling effects. The numbers overestimate the partitioning of ice with respect to the other classes due to two rationales: (1) the satellite sampling results in a specifically high measurement density at the highest latitudes (|φ|=80°-90°) where in the SH mid-winter the coldest temperature occur and the statistics suggests that ice is the most likely PSC type (up 50%). (2) Spectra at tangent heights below optical thick clouds are usually also flagged as cloudy and will most likely be classified as the overlying cloud because the emissions are dominated by the optically thick spectrum in the layer above. The respective spectrum may be even cloud-free or of a different cloud type, but is masked by the cloud layer above. The cloud scenarios of the CSDB show that optically thick spectra (CI<1.3) are most likely to observe for PSDs of ice clouds. Due to the large water abundance (3-5 ppmv) compared to the limited HNO_3 abundance (3-15 ppbv) in the stratosphere volume densities of ice can reach significantly larger values than NAT and STS. As a result of item (1) and (2) the amount of ice clouds can easily be overestimated by limb measurements, especially when the atmospheric conditions favours the frequent formation of optically thick ice clouds, which is typically expected for mid-SH-winter conditions (Jul/Aug).

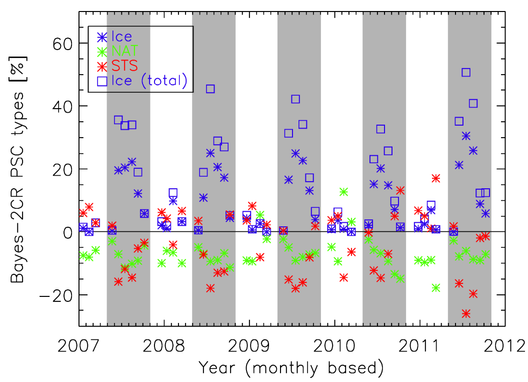

Figure 11: Differences in partitioning of the three PSC types between the new Bayesian classifier and the 2CR method based on all classified MIPAS spectra for each month of the years. SH analyses are highlighted by the grey shaded areas, NH data are in the white areas. In addition, the probability of the Bayes ice class with respect to all analysed PSC spectra is superimposed (blue open squares). This number visualises the relevance of ice clouds at the specific time of the PSC season. For the comparison, we added the Bayes STS_NAT class to the STS class, which is in-line with the definition of three classes attributed by the 2CR method (for details see text).

Atmos. Meas. Tech. Discuss., doi:10.5194/amt-2016-20, 2016
Manuscript under review for journal Atmos. Meas. Tech.
Published: 15 February 2016

4 Data analysis

We applied Bayesian classifier to the full MIPAS dataset from July 2002 to March 2012. The period includes a couple of longer data gaps caused by technical problems with the interferometer (e.g., Fischer et al., 2008), with the main gap between April and December 2004. However, the final dataset still provides excellent geographical and temporal coverage for 10 NH and 9 SH polar winters of day and night time observations. This gives the opportunity for detailed case studies of polar processes related to PSC formation as well as for the compilation of a unique pole-covering climatology of PSC types.

4.1 A case study of gravity wave induced PSC formation

Höpfner et al. (2006b) showed the importance of mountain waves (MW) over the Antarctic Peninsula for the formation of an Antarctic NAT belt that was observed for the first time by MIPAS in the SH winter 2003. Currently, scientific interest is growing for a better assessment of the importance of gravity waves on the formation process of PSCs and a better representation of these processes in CCMs for more precise ozone predictions (Alexander et al., 2013, Orr et al., 2015). The new data set of observations of PSC types for multiple SH and NH winter conditions up to pole may help to better constrain and validate new microphysical models describing the homogenous and heterogeneous formation processes for ice and NAT (e.g., Engel et al., 2013, Hoyle et al., 2013). These models are beyond the status of simple equilibrium schemes, which are still used in most CTMs and CCMs. A first study of using the new NAT scheme in the global chemical transport models CLaMS shows promising results (Grooß et al., 2014).

Figure 12 presents an example of the daily evolution of the PSC distribution of the Bayesian Classifier for June 2010. The coloured symbols represent the PSC classes, where in addition to the 3 main classes (ice, STS, NAT), the 3 mixed-types, unspecified, and optically thick clouds are also highlighted. Underlaid gridded 15 µm brightness temperature variances retrieved from AIRS are presented as a proxy for the gravity wave (GW) activity in the altitude range around 20-25 km (see Sec. 2). It is obvious that the first outbreak of orographic GWs on June 1 has no imprint on the formation of NAT clouds in the outer region of the polar vortex. Wind conditions and temperature development of the cold pole do not favour the formation of PSCs by temperature variations induced by this mountain wave event. In contrast, the June 11 event immediately creates signals for NAT clouds in the downstream region of the Antarctic Peninsula. Until around June 22 large areas of the polar vortex in the temperature regime well above T_{ice} are filled with cloud events attributed to NAT. Most of these NAT events seems to originate from transport processes along the superimposed Montgomery stream function. These contours represent roughly the streamlines of the geostrophic wind and the NAT clouds are along contours crossing the AP region. These observations are in line with the mountain-wave seeding hypothesis for PSCs as described and proofed with AIRS and MIPAS data by Eckermann et al. (2010) or to the MIPAS NAT-belt events in mid-June 2003 and 2008 previously reported by Höpfner et al. (2006b) and Lambert et al. (2012), respectively. Preliminary analyses for all MIPAS and AIRS SH observation suggest that generally the early winter conditions in mid-June facilitate meteorological conditions to form a mountain-wave induced NAT-belt (8 out of 10 winter). However, we also found similar sporadic outbreaks in the region of the Antarctic Peninsula in a couple of September observations. Those usually do not develop to the full extent of a NAT-belt, where a nearly complete

Atmos. Meas. Tech. Discuss., doi:10.5194/amt-2016-20, 2016
Manuscript under review for journal Atmos. Meas. Tech.
Published: 15 February 2016

ring of NAT clouds fills the outer region of the cold pole region inside the vortex. This case study demonstrates that the BC provides a physically reasonable classification in a well-defined meteorological setting.

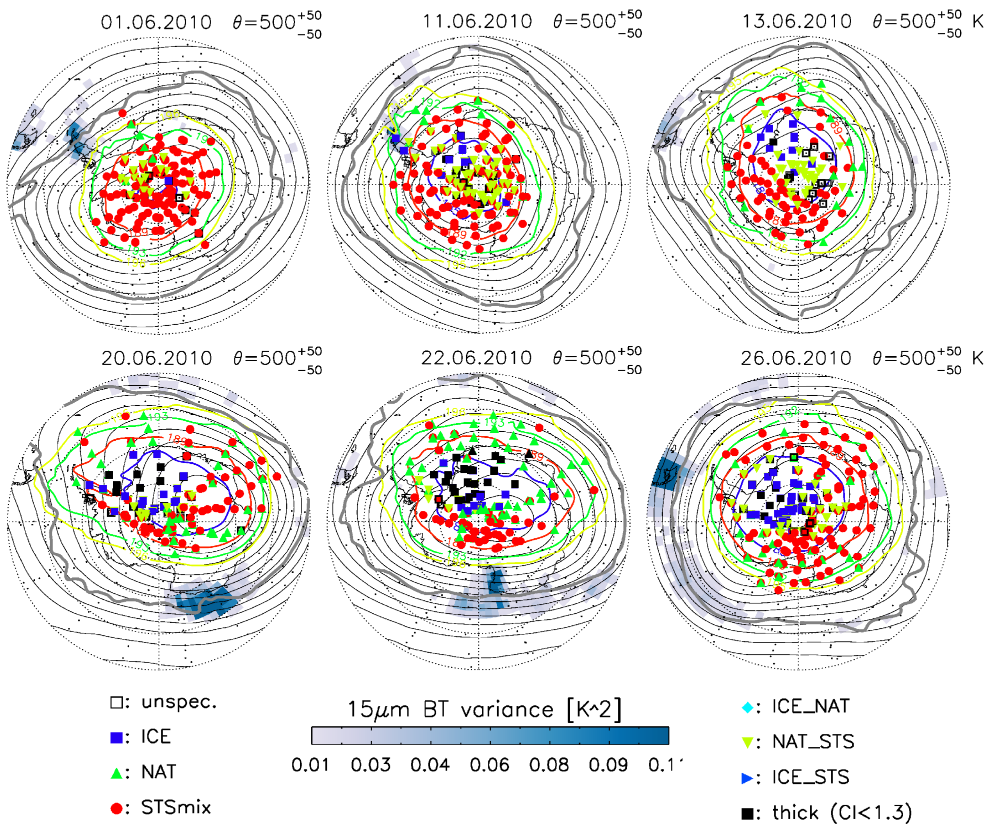

Figure 12: Coloured symbols represents daily PSC distribution of the Bayesian Classifier for June 1, 11, 13, 20, 22, and 26 in 2011 in the potential temperature altitude range 500K±50K equivalent to ~20 km geometric altitude. Black dots highlight the MIPAS profile location. Superimposed in colour-coded grid boxes with 4° longitude x 2° latitude resolution in the background show brightness temperature variances from AIRS as a proxy for GW activity in the lower stratosphere. Black contour lines represent the Montgomery stream function computed from ERA Interim (Dee et al., 2011) data and illustrate the large-scale geostrophic flow conditions. The potential vorticity-based vortex boundary is highlighted by a dark grey contour. In addition colour coded temperature contours represents the existing threshold temperatures T_{NAT}+2K, T_{NAT}, T_{STS} (estimated by (T_{NAT}+T_{ice})/2) and T_{ice} in yellow, green, red and blue for constant stratospheric values for HNO_3 (9 ppbv) and H_2O (4 ppmv) and according to the formula by Hanson and Mauersberger (1988), and Marti and Mauersberger (1993).

Atmos. Meas. Tech. Discuss., doi:10.5194/amt-2016-20, 2016
Manuscript under review for journal Atmos. Meas. Tech.
Published: 15 February 2016

Atmospheric Measurement Techniques Discussions

4.2 Overall behaviour of the new classification approach

The new PSC type classification approach for MIPAS provides data for the entire time of the Envisat mission (June 2002 – March 2012). With the restriction to tangent altitudes between 15 and 35 km, north and south of 55° and -55° latitude respectively, we found more than 14,000 PSC profiles out of 205,000 profiles in the NH and more than 108,000 profiles out of 255,000 in SH winter season. The PSC seasons are defined from November to March and from May to October, respectively. **Figure 13** summarises the classification into the main groups of cloud types (ice, NAT, STS, NAT_STS, and unknown) for Arctic and Antarctic winter conditions with respect to all potential PSC spectra of MIPAS. The total number of PSC spectra and the partitioning between the type classes highlight the general difference in the meteorological conditions between the northern and southern polar vortices. The much colder and prolonged cold pool region in the Antarctic favours a much more intensive vortex-wide PSC formation and significantly longer PSC season than in the Arctic. There, the temperatures are usually not low enough to form larger areas with ice PSCs. Consequently, the percentage of ice (4%) is significantly smaller than NAT (19%), and STS (72%) is the dominating cloud type in the NH winter. In contrast, the SH shows par-like conditions between the ice, NAT, and STS (31, 33, and 27%).

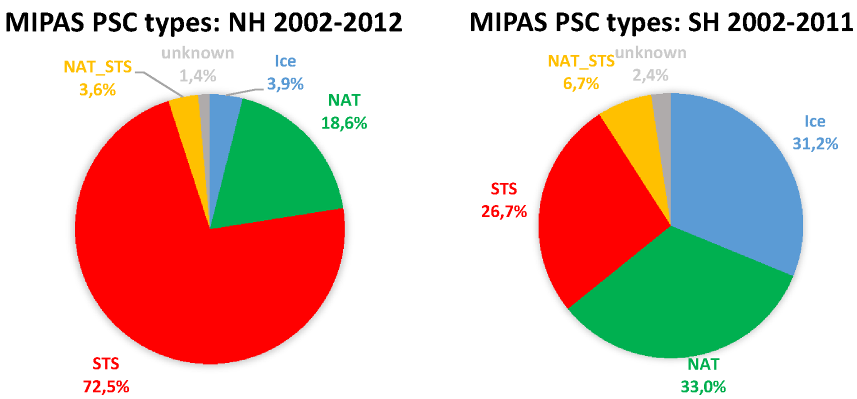

Figure 13: Breakdown of PSC types observed by MIPAS in the Arctic (Dec – Mar, left) and Antarctic (May – Oct, right) from 2002 to 2012. The percentages are averages over 10 and 9 seasons respectively, and relate to the total number of analysed spectra north/south of 55°/-55° latitude. Spectra more than 6 km below the actual CTH in the profile are not taken into account. In total 44,622 cloudy spectra for the NH and 317,699 for SH are analysed.

In comparison to the statistics of Pitts et al. (2011) for four winter of CALIOP measurements (2006-2010) in the SH, MIPAS shows significantly larger ice abundance (31%) than CALIOP (12%, Fig. 3 in Pitts et al, 2011), whereas in the NH both

Atmos. Meas. Tech. Discuss., doi:10.5194/amt-2016-20, 2016
Manuscript under review for journal Atmos. Meas. Tech.
Published: 15 February 2016

instruments show a very similar partitioning of 3.9% and 3.2%, respectively. The large SH difference is only partly a surprising fact and not necessarily related to potential differences in detection sensitivity for specific PSC and mixed-PSC types between the different measurement techniques. Most of this difference can be attributed to the different latitudinal coverage of both instruments. MIPAS has the advantage to cover the complete polar cap, whereas CALIOP is restricted to a maximum latitude of 82°. Overlapping orbits at high latitudes increase the measurement density in particular for MIPAS. Together with the fact that the SH cold pool for most winters is centred exactly over the south pole, the large abundance of ice clouds observation in SH for MIPAS can be explained in large parts by differences in the sampling and orbit geometry between MIPAS and CALIOP. As a test, we restricted the MIPAS observations to a maximum latitude of 80° N/S and applied the classification to the same winters of the CALIOP statistics. The result shows a reduction for the ice partition from 31% to 20%. However, the remaining value is still a significantly larger ice fraction than in the CALIOP analysis (12%) and indicates more fundamental limitations and difficulties for comparisons between CALIOP and MIPAS. A more detailed discussion of these limitations is presented in the next section.

4.3 MIPAS-CALIOP coincidence comparison

For the verification of the MIPAS PSC classification, only ground and space-based lidar PSC classification are available. Due to the fundamentally different measurement geometries, affecting vertical and horizontal resolution as well measurement sensitivity, the potential for meaningful comparisons is limited. Since CALIOP is the only other instrument with similar global and temporal coverage as MIPAS, we decided to compare only with CALIOP.

The high vertical and along-track resolution and a well-established classification scheme (Pitts et al., 2009) makes the CALIOP dataset valuable for PSC research (e.g., Peter and Grooß, 2013, WMO, 2014). The good temporal overlap of the CALIOP dataset with the MIPAS measurements (07/2007-03/2012) allows a detailed comparison with the new classification approach. The high measurement frequency for both satellites and similar coverage results in a high statistical significance for a comparison in spite of quite stringent coincidence criteria.

4.3.1 Principles and sensitivities of nadir-limb comparisons

The extremely highly resolved vertical and along-track measurements of CALIOP result in a kind of hyper-sampling of PSC structures compared to the MIPAS observations. MIPAS has to cope with the so-called limb path smearing effect (Spang et al., 2012, 2015). **Figure 14** illustrates this effect for an example where MIPAS and CALIOP measure in the same orbit plane. Such a constellation is regularly achieved in the A-Train constellation for several of the NASA Earth observation satellites and instruments (e.g., CALIPSO and MLS), but is not the situation for the MIPAS and CALIOP orbits (similar inclination but different orbit latitudes and equator crossing times). For better illustration of a typical coincidence, **Figure 14** shows the along-track CALIOP PSC type observations overlaid with the MIPAS line of sights of several limb scans along the CALIOP orbit track, where we assume that both satellites operate in the same orbit plane. Usually a coincidence is characterised by a crossing point of both orbits (profile with coloured squares for the MIPAS classification result). The next and the previous MIPAS

Atmos. Meas. Tech. Discuss., doi:10.5194/amt-2016-20, 2016
Manuscript under review for journal Atmos. Meas. Tech.
Published: 15 February 2016

Atmospheric Measurement Techniques Discussions

profiles (thin lines) are already outside of the defined match radius (Δx=100 km). The long limb path through atmosphere causes the limb smearing effect, where the information on the start and endpoint of the cloud along the line of sight is not retrievable from a single limb scan. The detection of a cloudy spectrum is attributed to the original tangent height although the entrance in the cloud along the line of sight can be located in front of or behind the tangent point. This results in an uncertainty for the retrieved CTH. Spectra with tangent heights below the CTH might falsely be indicated as cloudy due to the cloud layer above (e.g., Höpfner et al., 2009). In contrast, the long limb path is a great advantage for the observation of optically very thin clouds and aerosols, because the measurement integrates the signal along the line of sight.

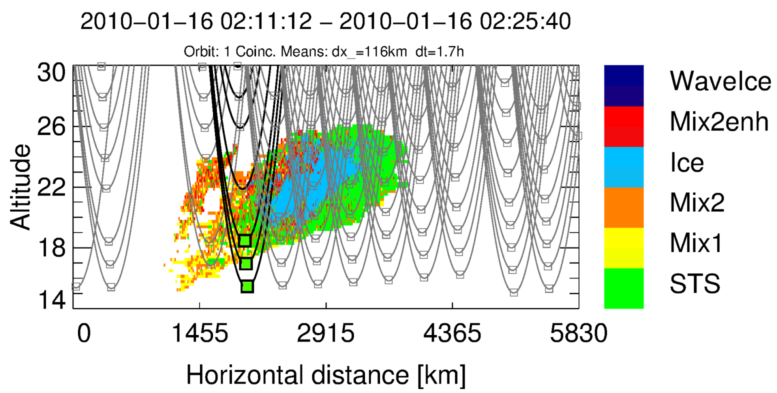

Figure 14: Visualisation of the MIPAS limb paths (black lines) and a coincident MIPAS profile (coloured black-framed squares, other profiles do not fulfil the coincidence criteria) compared to the CALIOP high-resolution nadir measurements of PSC types (coloured pixels). The colour bar refers to the CALIOP PSC type classification. For details see text.

Spang et al. (2015) showed that an ADP > 10^7 µm^2/cm^2 is detectable for such as MIPAS (assuming a completely filled vertical and cross-track FOV). This threshold (ADP$_{thres}$) is equivalent to an ice water path of 0.3 g/m^2, which corresponds to a cloud layer with 100 km and 1 km horizontal extent to an IWC of 0.003 mg/m^3 and 0.3 mg/m^3, respectively. These small water concentrations illustrate the extreme sensitivity of the IR limb cloud detection even if the IWC is concentrated in a cloud that only partially fills the FOV. For the estimates, we assumed a cloud filling the complete cross-track and vertical FOV and a constant effective radius (R_{eff}) of 10 µm. A thinner cloud layer will almost linearly increase the detection threshold, depending on where the cloud layer is placed in the FOV of MIPAS (Spang et al., 2015).

We investigated potential differences in the detection sensitivity for both instruments in more detail. For the standard archived V1-00 CALIOP PSC Mask the estimated minimum detectable STS volume density is 0.25 µm^{3}cm^{-3} (L. Poole, personnel communication). This value is applicable at 180 m vertical x 135 km horizontal resolution, the coarsest mean values applied in the dataset to improve the signal to noise ratio. The MIPAS detection sensitivity for STS is a volume density in the order of 0.45 µm^{3}cm^{-3} and is based on the simulated spectra of the CSDB and the compact correlation between CI and log(VDP) with an applied threshold values of CI_{thres}=4.5 in the detection algorithm and the identical horizontal integration length through the cloud. Consequently, both instruments show a similar detection sensitivity. However, not all coincidences for the CALIOP measurements have such a long horizontal extent of 135 km and observations of the same cloud structures by both instruments may not have the same horizontal extent in the individual measurement due the different orbit geometry (see above). The MIPAS detection threshold is independent on any averaging due to the inertial integrating measurement technique in contrast to the CALIOP product. This allows a better detection sensitivity than CALIOP under certain conditions, for example for optically thin clouds close to and below the threshold value of CALIOP with a longer horizontal extent along the MIPAS line of sight than the maximum 135 km averaging of the CALIOP data processing.

4.3.2 Coincidence statistics

For the coincidence comparisons we applied very stringent miss-time (Δt = 2 hours) and miss-distance (Δx = 100 km) criteria. This implies observation geometries where one MIPAS profile is coincident with an orbit segment of hundreds of individual CALIOP measurements (**Figure 14**). For example a maximum horizontal extent of 200 km (2 x Δx) combined with the vertical FOV of MIPAS of 3 km results in a maximum number of CALIOP observations (pixels) of (200 km / 5 km) x (3 km / 0.18 km) = 680 pixels. Instead of analysing these large numbers of coincident CALIOP pixels separately, we combined the whole set of CALIOP pixels and compare the most likely PSC type with the corresponding MIPAS observation. This MIPAS-like CALIOP PSC type is estimated by assigning the CALIOP type with the maximum count number in the ensemble. Caveats of this approach, which may bias the coincidence comparison for ice, are discussed below. A mean CALIOP coincidence is attributed as 'no-cloud' (none-cloudy) only if each coincident CALIOP pixel shows no cloud indication at all. In addition, we took care about the MIPAS difficulties to quantify the vertical extent of the cloud below the CTH and restricted the analysis to up to two altitude steps below the CTH.

Figure 15 summarises the count statistics for each specific PSC class for CALIOP and for MIPAS with respect to the PSC classes of the coincident measurement of the corresponding instrument. We selected a SH winter mean of three successive winters for the comparison, which results already in an excellent count statistics of more than 12,000 MIPAS profiles with coincident CALIOP information.

Taking the CALIOP measurements for reference (**Figure 15**, top) the ice classification of MIPAS (>97%) seems to perfectly match with the CALIOP ice class. Also promising, the small number of CALIOP wave-ice (Sec. 2.3) agrees very well with MIPAS ice (7 out of 8 events). The Mix2-enhanced class (most likely NAT clouds with high volume densities and/or ice clouds) is dominated by MIPAS ice coincidences (80%) with a certain fraction of NAT (~10%). CALIOP Mix1 and Mix2 classes are largely assigned to the MIPAS NAT class with 70% and 56% respectively. For STS CALIOP provides a very robust classification, because STS is the only PSC type without depolarisation. However, the MIPAS classifier distributes the partitioning nearly equally over the different classes, with 44% STS and 16% NAT_STS, whereas 40% were attributed to ice and NAT. For the 2381 coincidences where CALIOP shows no indications for clouds, MIPAS detects only in ~40% of the events non-cloudy conditions as well, but in total more than 55% NAT and STS_{mix} spectra. This part of the comparison suggests

Atmos. Meas. Tech. Discuss., doi:10.5194/amt-2016-20, 2016
Manuscript under review for journal Atmos. Meas. Tech.
Published: 15 February 2016

Atmospheric Measurement Techniques
Discussions

a higher detection sensitivity for MIPAS than for the CALIOP product. But the difference to CALIOP can also be an indication for a kind of hypersensitivity in the MIPAS cloud detection algorithm, for example if the method detects optically very thin background aerosol as PSC. The spectral dependence of sulfuric acid has much more similarities to NAT and STS compared to ice, and consequently falsely detected aerosol should be most likely classified as NAT or STS (55%) and not as ice (<5%).

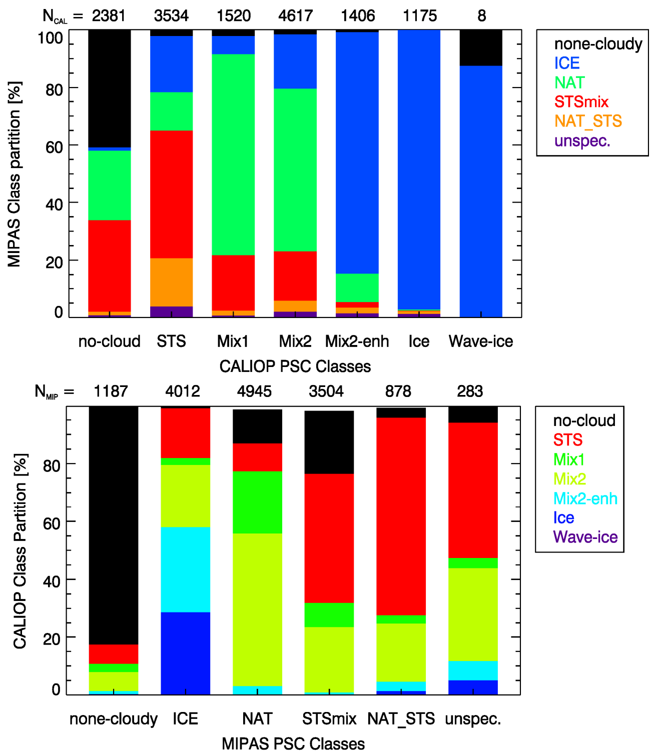

Figure 15: The MIPAS-CALIOP coincidence count statistics of the mean SH winter seasons 2009-2011 (May-Oct). A miss-time of $\Delta t < 2$ hours and miss-distance of $\Delta x < 100$ km is applied together with the estimation of an MIPAS-like mean CALIOP type and only observation above 16 km are taken into account (for details see text). **Top**: Partitioning of the coincident MIPAS classes for the coincident CALIOP classification results. **Bottom**: Partitioning of the coincident CALIOP classification for the MIPAS classes. Numbers on top of the coloured bars indicate the number of observation of the corresponding PSC class.

Taking the MIPAS classes as the reference (**Figure 15**, bottom), the comparison of the non-cloudy events shows better agreement than the CALIOP reference comparison (**Figure 15**, top) with only 20% of the CALIOP coincidences classified as cloudy compared to 60% of MIPAS coincidences are classified as cloudy for no-cloud CALIOP conditions. For the other CALIOP classes (**Figure 15**, bottom) the MIPAS ice class events show only in 30% of the coincidences a CALIOP ice class. The NAT class coincidences are distributed mainly to two CALIOP types, Mix1 (21%) and Mix2 (53%), and only minor contributions for STS (<10%), Mix2-enh (<3%) and nearly no indication for ice (0.1%). For the STS_{mix} class 45% of the CALIOP coincidences are classified as STS, whereby only Mix2 (may include larger number densities of NAT) of the CALIOP mixed-type classes contributes significantly (23%). Here a relatively large part of 22% are no-cloud events for CALIOP.

The impression of large differences in the ice classification between both instruments taken MIPAS as reference might be created by different sensitivities for ice, NAT, and STS of the two instruments. This causes difficulties in the case of observations of mixed-type clouds along the limb path. Due to the much bigger abundance of water vapour (~5 ppmv) in the stratosphere compared to nitric acid (5-15 ppbv) and consequently higher volume densities, ice clouds create significantly stronger signals in the primary measurement quantities of MIPAS and CALIOP (IR radiances and attenuated backscatter, respectively). Therefore, already a minor partition of CALIOP ice pixel in the MIPAS-like FOV box creates such a strong signal that these emissions can dominate the total radiances integrated along the line of sight and measured by MIPAS.

Table 3 investigates the effect of varying ice fraction (f_{ICE}) threshold in the MIPAS-like FOV mean information for the coincident CALIOP measurements. We applied a simple approach to test the sensitivity of the ice fraction for the MIPAS ice class coincidences by changing the threshold condition from the original f_{ICE} = 0.5 down to 0.001. Obviously, this reduction has a very strong influence on the comparison of the MIPAS ice class with the CALIOP ice class. Reducing f_{ICE} from 0.3 to 0.1 the ice amount is increased to ~50% by a reduction in the Mix2-enh class (attributed to mixed-type of NAT and ice, Pitts et al, 2012). Finally, the ice partition increases up to >85% for a reduction of f_{ICE} down to 0.001 at the expenses of the Mix2 class. An ice fraction f_{ICE} = 0.001 represents a minimum just one cloudy ice pixel in the 3 km x 200 km MIPAS-like FOV box. The sensitivity study indicates an overemphasis effect for ice in the observation of mixed-type clouds for the MIPAS Bayesian classifier, which needs consideration in the comparison. It seems difficult to quantify a representative threshold value precisely. In future studies radiative transfer model calculations with different mixtures of PSC types could help to better estimate the threshold values.

Table 3: MIPAS-like PSC types partitioning for CALIOP with respect to ice fraction (f_{ICE}), f_{ICE} = 0.5 represents a fraction >50%, type contribution is given in %.

f_{ICE}	no-cloud	STS	Mix1	Mix2	**Ice**	Mix2-enh	Wave-ice
0.50	0.67	17.10	2.37	21.54	**28.44**	29.36	0.17
0.30	0.67	16.65	2.37	21.54	32.28	25.87	0.27
0.10	0.67	12.56	2.29	19.39	**50.72**	13.01	1.00
0.05	0.67	10.59	2.22	17.72	59.12	7.58	1.74
0.01	0.62	6.16	1.97	12.41	73.98	1.47	3.04
0.001	0.62	3.56	1.55	6.93	**86.69**	0.30	0.00

5 Summary

We presented a new classification approach for different polar stratospheric clouds. The approach is developed for IR limb measurements by the MIPAS instruments on board ESAs Envisat satellite. The so-called Bayesian classifier combines the information content of various correlation diagrams of colour ratios and brightness temperature differences in the wavenumber region 790 to 1450 cm^{-1} covering several atmospheric window regions. The classifier estimates the most likely probability that one of the three PSC types (ice, NAT, or STS) is dominating the spectral characteristics in a MIPAS spectrum affected by clouds. In addition, mixed-type clouds are defined, where none of the three type probabilities is > 50% but two are in the intermediate range of 40-50%.

In a first comparison with coincident CALIOP measurements excellent count statistics was achieved over several PSC seasons even though we applied restrictive miss time and miss distance criteria. Overall, the comparison shows good consistency between both instruments, even though the PSC classes are based on different measurement quantities, and the effect of mixed-type clouds can be very different for each instrument. The latter fact explains in part differences in the classification of mixed-type clouds. Especially the complementary viewing geometries (nadir/limb), whereby MIPAS always integrates over a large horizontal distance and CALIOP represents a more hyper-sampled pixel measurement, creates some general caveats for a comparison of cloud types retrieved from both types of instrument.

The entire MIPAS measurement period from July 2002 to April 2013 is processed with the Bayesian classifier and constitutes a unique data set of day and night time PSC measurements up to the poles. Climatological mean winter statistics for PSC type occurrence frequencies and height resolved statistics of PSC area of the polar vortex over all winters can now be analysed. The dataset has the potential to be used for validation of current chemical transport models with sophisticated microphysical schemes, or to improve climate chemistry model with more simple heterogeneous chemistry modules. In this way, the dataset can potentially help to improve the predictability of the future polar stratospheric ozone trends by these models.

In a case study for the SH polar vortex using MIPAS PSC data together with AIRS analyses on the gravity wave activity over Antarctica, we showed the potential for the synergetic use of various remote sensing instruments to explore mountain wave induced PSC formation. This capability will be investigated in more depth over multiple years in an ongoing study by combining AIRS and MIPAS data together with results from the UK Unified Model including a parameterisation for sub-grid mountain wave processes (Orr et al., 2015). This may help to improve global models with respect to this only rarely considered effect in CCM and CTMs.

Acknowledgement

The authors like to thank ESA for providing MIPAS level 1b data and funding of the MIPclouds study as well as NASA for providing CALIOP data. R.S. thanks Ines Tritscher (FZJ) for support with the visualisation of the CALIOP data. Part of this work is inspired by discussions during the 1st PSC Initiative (PSCi) workshop funded by the International Space Science Institute (ISSI) in Bern, Switzerland.

References

Achtert, P., and Tesche, M.: Assessing lidar-based classification schemes for polar stratospheric clouds based on 16 years of measurements at Esrange, Sweden, J. Geophys. Res., 119, 1386-1405, doi:10.1002/2013JD020355, 2014.

Alexander, S. P., Klekociuk, A. R., McDonald, A. J., and Pitts, M. C.: Quantifying the role of orographic gravity waves on polar stratospheric cloud occurrence in the Antarctic and the Arctic, J. Geophys. Res. Atmos., 118, 11,493–11,507, doi:10.1002/2013JD020122, 2013.

Arnone, E., Castelli, E., Papandrea, E., Carlotti, M., and Dinelli, B. M.: Extreme ozone depletion in the 2010–2011 Arctic winter stratosphere as observed by MIPAS/ENVISAT using a 2-D tomographic approach, Atmos. Chem. Phys., 12, 9149-9165, doi:10.5194/acp-12-9149-2012, 2012.

Aumann, H. H., Chahine, M. T., Gautier, C., Goldberg, M. D., Kalnay, E., McMillin, L. M., Revercomb, H., Rosenkranz, P. W., Smith, W. L., Staelin, D. H., Strow, L. L., and Susskind, J.: AIRS/AMSU/HSB on the Aqua Mission: Design, Science Objective, Data Products, and Processing Systems, in: IEEE Trans. Geosci. Remote Sens., 41, 253-264, 2003.

Avery, M., Winker, D., Heymsfield, A., Vaughan, M., Young, S., Hu, Y., and Trepte, C.: Cloud ice water content retrieved from the CALIOP space-based lidar, Geophys. Res. Lett., 19, L05808, doi:10.1029/2011GL050545, 2012.

Biermann, U. M., Luo, B. P., and Peter, T.: Absorption spectra and optical constants of binary and ternary solutions of H_2SO_4, HNO_3, and H_2O in the mid infrared at atmospheric temperatures, J. Phys. Chem. (A), 104, 783–793, 2000.

Carslaw, K. S., Wirth, M., Tsias, A., Luo, B. P., Dörnbrack, A., Leutbecher, M ., Volkert, H., Renger, W., Bacmeister, J.T., Reimer, E., Peter, T.: Increased stratospheric ozone depletion due to mountain-induced atmospheric waves, Nature, 391, 675-678, DOI:10.1038/35589, 1998.

Chahine, M. T., Pagano, T. S., Aumann, H. H., Atlas, R., Barnet, C., Blaisdell, J., Chen, L., Divakarla, M., Fetzer, E. J., Goldberg, M., Gautier, C., Granger, S., Hannon, S., Irion, F. W., Kakar, R., Kalnay, E., Lambrigtsen, B. H., Lee, S., Marshall, J. L., McMillan, W. W., McMillin, L., Olsen, E. T., Revercomb, H., Rosenkranz, P., Smith, W. L., Staelin, D., Strow, L. L., Susskind, J., Tobin, D., Wolf, W., and Zhou, L.: AIRS: improving weather forecasting and providing new data on greenhouse gases, B. Am. Meteorol. Soc., 87, 911-926, 2006.

Clarisse, L., Coheur, P.-F., Prata, F., Hadji-Lazaro, J., Hurtmans, D., and Clerbaux, C.: A unified approach to infrared aerosol remote sensing and type specification, Atmos. Chem. Phys., 13, 2195-2221, doi:10.5194/acp-13-2195-2013, 2013.

Atmospheric Measurement Techniques Discussions

Dee, D. P., Uppala, S. M., Simmons, A. J., Berrisford, P., Poli, P., Kobayashi, S., Andrae, U., Balmaseda, M. A., Balsamo, G., Bauer, P., Bechtold, P., Beljaars, A. C. M., van de Berg, L., Bidlot, J., Bormann, N., Delsol, C., Dragani, R., Fuentes, M., Geer, A. J., Haimberger, L., Healy, S. B., Hersbach, H., Holm, E. V., Isaksen, L., Kallberg, P., Koehler, M., Matricardi, M., McNally, A. P., Monge-Sanz, B. M., Morcrette, J. J., Park, B. K., Peubey, C., de Rosnay, P., Tavolato, C., Thepaut, J. N., and Vitart, F.: The ERA-Interim reanalysis: configuration and performance of the data assimilation system, Q. J. R. Meteorol. Soc., 137, 553-597, doi:10.1002/qj.828, 2011.

Di Liberto, L., Cairo, F., Fierli, F., Di Donfrancesco, G., Viterbini, M., Deshler, T., and Snels, M.: Observation of polar stratospheric clouds over McMurdo (77.85°S, 166.67°E) (2006–2010), J. Geophys. Res. Atmos., 119, doi:10.1002/2013JD019892, 2014.

Drdla, K. and Müller, R.: Temperature thresholds for chlorine activation and ozone loss in the polar stratosphere, Annales Geophysicae, 30, 1055–1073, doi:10.5194/angeo-30-1055-2012, 2012.

Eckermann, S. D., Hoffmann, L., Höpfner, M., Wu, D. L., and Alexander, M. J.: Antarctic NAT PSC belt of June 2003: Observational validation of the mountain wave seeding hypothesis, Geophys. Res. Lett., 36, L02807, doi:10.1029/2008GL036629, 2009.

Engel, I., Luo, B. P., Pitts, M. C., Poole, L. R., Hoyle, C. R., Grooß, J.-U., Dörnbrack, A., and Peter, T.: Heterogeneous formation of polar stratospheric clouds – Part 2: Nucleation of ice on synoptic scales, Atmos. Chem. Phys., 13, 10769-10785, doi:10.5194/acp-13-10769-2013, 2013.

Eyring, V., et al.: Long-term ozone changes and associated climate impacts in CMIP5 simulations, J. Geophys. Res. Atmos., 118, 5029–5060, doi:10.1002/jgrd.50316, 2013.

Fahey, D. W., Gao, R. S., Carslaw, K. S., Kettleborough, J., Popp, P. J., Northway, M. J., Holecek, J. C., Ciciora, S. C., McLaughlin, R. J., Baumgardner, D. G., Gandrud, B., Wennberg, P. O., Dhaniyala, S., McKinney, K., Peter, T., Salawitch, R. J., Bui, T. P., Elkins, J. W., Webster, C. R., Atlas, E. L., Jost, H., Wilson, J. C., Herman, R. L., and Kleinbohl, A: The detection of large HNO_3-containing particles in the winter Arctic stratosphere, Science, 291, 1026–1031, doi: 10.1126/science.1057265 2001.

Fischer, H., Birk, M., Blom, C., Carli, B., Carlotti, M., von Clarmann,, T., Delbouille, L., Dudhia, A., Ehhalt, D., Endemann, M., Flaud, J. M., Gessner, R., Kleinert, A., Koopman, R., Langen, J., L´opez-Puertas, M., Mosner, P., Nett, H., Oelhaf, H., Perron, G., Remedios, J., Ridolfi, M., Stiller, G., and Zander, R.: MIPAS: an instrument for atmospheric and climate research, Atmos. Chem. Phys., 8, 2151–2188, doi:10.5194/acp-8-2151-2008, 2008.

Gerber, E.P., and Son, S.-W.: Quantifying the summertime Austral jet stream and Hadley Cell response to stratospheric ozone and greenhouse gases, J. Clim., 27, 5538-5559, 2014.

Grainger, R. G., Peters, D. M., Thomas, G. E., Smith, A. J. A., Siddans, R., Carboni, E., and Dudhia, A.: Measuring Volcanic Plume and Ash Properties from Space, in: Remote-sensing of Volcanoes and Volcanic Processes: Integrating Observation and Modelling, edited by: Pyle, D., Mather, T., and Biggs, J., The Geological Society Special Publication 380, doi:10.1144/SP380.7, 2013.

Griessbach, S., Hoffmann, L., Spang, R., and Riese, M.: Volcanic ash detection with infrared limb sounding: MIPAS observations and radiative transfer simulations, Atmos. Meas. Tech., 7, 1487-1507, doi:10.5194/amt-7-1487-2014, 2014.

Grooß, J.-U., Engel, I., Borrmann, S., Frey, W., Günther, G., Hoyle, C. R., Kivi, R., Luo, B. P., Molleker, S., Peter, T., Pitts, M. C., Schlager, H., Stiller, G., Vömel, H., Walker, K. A., and Müller, R.: Nitric acid trihydrate nucleation and denitrification in the Arctic stratosphere, Atmos. Chem. Phys., 14, 1055-1073, doi:10.5194/acp-14-1055-2014, 2014.

Grossmann, K. U., Offermann, D., Gusev, O., Oberheide, J., Riese, M., and Spang, R.: The CRISTA-2 mission, J. Geophys. Res., 107(D23), 8173, doi:10.1029/2001JD000667, 2002.

Hanson, D. and Mauersberger, K.: Solubility and equilibrium vapour pressures of HCl dissolved in polar stratospheric cloud materials - Ice and the trihydrate of nitric acid, Geophys. Res. Lett., 15, 1507–1510, doi:10.1029/GL015i013p01507, 1988.

Höpfner, M., Oelhaf, H., Wetzel, G., Friedl-Vallon, F., Kleinert,, A., Lengel, A., Maucher, G., Nordmeyer, H., Glatthor, N., Stiller, G. P., von Clarmann, T., Fischer, H., Kr¨oger, C., and Deshler, T.: Evidence of scattering of tropospheric radiation by PSCs in mid-IR limb emission spectra: MIPAS–B observations and KOPRA simulations, Geophys. Res. Lett., 29, doi:10.1029/2001GL014443, 2002.

Höpfner, M., Study on the impact of polar stratospheric clouds on high resolution mid-IR limb emission spectra, J. Quant. Spectrosc. Radiat. Transfer, 83, 1, 93-107, 2004.

Höpfner, M., Luo, B. P., Massoli, P., Cairo, F., Spang, R., Snels, M., Donfrancesco, G. D., Stiller, G., von Clarmann, T., Fischer, H., and Biermann, U.: Spectroscopic evidence for NAT, STS, and ice in MIPAS infrared limb emission measurements of polar stratospheric clouds, Atmos. Chem. Phys., 6, 1201–1219, doi:10.5194/acp-6-1201-2006, 2006a.

Höpfner, M., Larsen, N., Spang, R.; Luo, B. P.; Ma, J., Svnedsen, S.H., Eckermann, S. D., Knudsen, B., Massoli, P., Cairo, F., Stiller, G., von Clarmann, T., Fischer, H., MIPAS detects Antarctic stratospheric belt of NAT PSCs caused by mountain waves, Atmospheric Chemistry and Physics, 6, 1221–1230, doi:10.5194/acp-6-1221-2006, 2006b.

Höpfner, M., Pitts, M. C., and Poole, L. R., Comparison between CALIPSO and MIPAS observations of polar stratospheric clouds, J. Geophys. Res., 114, D00H05, doi:10.1029/2009JD012114, 2009.

Hoffmann, L., Xue, X., and Alexander, M. J.: A global view of stratospheric gravity wave hotspots located with Atmospheric Infrared Sounder observations, J. Geophys. Res., 118, 416-434, doi:10.1029/2012JD018658, 2013.

Hoffmann, L., Alexander, M. J., Clerbaux, C., Grimsdell, A. W., Meyer, C. I., Rößler, T., and Tournier, B.: Intercomparison of stratospheric gravity wave observations with AIRS and IASI, Atmos. Meas. Tech., 7, 4517-4537, doi:10.5194/amt-7-4517-2014, 2014.

Hoyle, C. R., Engel, I., Luo, B. P., Pitts, M. C., Poole, L. R., Grooß, J.-U., and Peter, T.: Heterogeneous formation of polar stratospheric clouds – Part 1: Nucleation of nitric acid trihydrate (NAT), Atmos. Chem. Phys., 13, 9577-9595, doi:10.5194/acp-13-9577-2013, 2013.

Hurley, J., Dudhia, A., and Grainger, R. G.: Retrieval of macrophysical cloud parameters from MIPAS: algorithm description, Atmos. Meas. Tech., 4, 683-704, doi:10.5194/amt-4-683-2011, 2011.

Lambert, A., Santee, M. L., Wu, D. L., and Chae, J. H.: A-train CALIOP and MLS observations of early winter Antarctic polar stratospheric clouds and nitric acid in 2008, Atmos. Chem. Phys., 12, 2899-2931, doi:10.5194/acp-12-2899-2012, 2012.

Li, J, Menzel, W. P., Yang, Z. D., Frey, R. A., Ackerman, S. A.: High-spatial-resolution surface and cloud-type classification from MODIS multispectral band measurements. JOURNAL OF APPLIED METEOROLOGY, 42(2), 204-226, 2003.

Livesey, N. J., Snyder, W. V., Read, W. G., and Wagner, P. A.: Retrieval algorithms for the EOS Microwave Limb Sounder (MLS), IEEE T. Geosci. Remote, 44, 1144–1155, 2006.

Manney, G. L., Santee M. L., Rex, M., et al.: Unprecedented Arctic ozone loss in 2011, Nature, 478, 469–475, doi:10.1038/nature10556, 2011.

Marti, J. and Mauersberger, K.: Laboratory simulations of PSC particle formation, Geophys. Res. Lett., 20, doi: 10.1029/93GL00083, 1993.

Mie, G.: Beiträge zur Optik trüber Medien, speziell kolloidaler Metallösungen, Annalen der Physik 330 (3): 377–445, doi:10.1002/andp.19083300302, 1908.

Offermann, D., Grossmann, K. U., Barthol, P., Knieling, P., Riese, M., and Trant, R.: The CRyogenic Infrared Spectrometers and Telescopes for the Atmosphere (CRISTA) experiment and middle atmosphere variability, J. Geophys. Res., 104, 16,311-16,325, 1999.

Orr, A., Hosking, J. S., Hoffmann, L., Keeble, J., Dean, S. M., Roscoe, H. K., Abraham, N. L., Vosper, S., and Braesicke, P.: Inclusion of mountain-wave-induced cooling for the formation of PSCs over the Antarctic Peninsula in a chemistry–climate model, Atmos. Chem. Phys., 15, 1071-1086, doi:10.5194/acp-15-1071-2015, 2015.

Peter, T., and Grooß, J.-U.: Polar Stratospheric Clouds and Sulfate Aerosol Particles: Microphysics, Denitrification and Heterogeneous chemistry, in *Stratospheric Ozone Depletion and Climate Change*, ed. Rolf Müller, RSC Publishing, 2011, ISBN 978-1-84973-002-0, p. 108-144, 2012.

Polvani, L. M., Waugh, D.W., Correa, G. J. P., and Son, S.-W.: Stratospheric ozone depletion: the main driver of 20th Century atmospheric circulation changes in the Southern Hemisphere, J. Climate, 24, 795-812, 2011.

Pitts, M. C., Poole, L. R., and Thomason, L. W.: CALIPSO polar stratospheric cloud observations: second-generation detection algorithm and composition discrimination, Atmos. Chem. Phys., 9, 7577-7589, doi:10.5194/acp-9-7577-2009, 2009.

Pitts, M. C., Poole, L. R., Dörnbrack, A., and Thomason, L. W.: The 2009-2010 Arctic polar stratospheric cloud season: a CALIPSO perspective, Atmos. Chem. Phys., 11, 2161–2177, doi:10.5194/acp-11-2161-2011, 2011.

Pitts, M. C., Poole, L. R., Lambert, A., and Thomason, L. W.: An assessment of CALIOP polar stratospheric cloud composition classification, Atmos. Chem. Phys., 13, 2975-2988, doi:10.5194/acp-13-2975-2013, 2013.

Polvani, L. M., Waugh, D. W., Correa, G. J. P., and Son S.-W.: Stratospheric Ozone Depletion: The Main Driver of Twentieth-Century Atmospheric Circulation Changes in the Southern Hemisphere. J. Climate, 24, 795–812, doi: http://dx.doi.org/10.1175/2010JCLI3772.1, 2011.

Raspollini, P., Carli, B., Carlotti, M., Ceccherini, S., Dehn, A., Dinelli, B. M., Dudhia, A., Flaud, J.-M., López-Puertas, M., Niro, F., Remedios, J. J., Ridolfi, M., Sembhi, H., Sgheri, L., and von Clarmann, T.: Ten years of MIPAS measurements with ESA Level 2 processor V6 – Part 1: Retrieval algorithm and diagnostics of the products, Atmos. Meas. Tech., 6, 2419-2439, doi:10.5194/amt-6-2419-2013, 2013.

Rex, M., Salawitch, R. J., von der Gathen, P., Harris, N. R. P., Chipperfield, M. P., and Naujokat, B.: Arctic ozone loss and climate change, Geophys. Res. Lett., 31, L04116, doi:10.1029/2003GL018844, 2004.

Sembhi, H., Remedios, J., Trent, T., Moore, D. P., Spang, R., Massie, S., and Vernier, J.-P.: MIPAS detection of cloud and aerosol particle occurrence in the UTLS with comparison to HIRDLS and CALIOP, Atmos. Meas. Tech., 5, 2537-2553, doi:10.5194/amt-5-2537-2012, 2012.

Shibata, T., Iwasaka, Y., Fujiwara, M., Hayashi, M., Nagatani, M., Shiraishi, K., Adachi, H., Sakai, T., Susumu, K., and Nakura, Y.: Polar stratospheric clouds observed by lidar over Spitsbergen in the winter 1994/1995: Liquid particles and vertical ‘‘sandwich’’ structure, J. Geophys. Res., 102, 10,829–10,840, 1997.

Solomon, S.: Stratospheric ozone depletion: a review of concepts and history, Rev. Geophys., 37, 275–316, 1999.

Spang R., and Remedios, J., Observations of a distinctive infra-red spectral feature in the atmospheric spectra of polar stratospheric clouds measured by the CRISTA instrument, Geophys. Res. Lett., 30, 1875, 2003.

Spang, R., Remedios, J. J., and Barkley, M., Colour Indices for the Detection and Differentiation of Cloud Types in Infra-red Limb Emission Spectra, Adv. Space Res., 33, pp.1041–1047, 2004.

Spang, R., Remedios, J. J., Kramer, L. J., Poole, L. R., Fromm, M. D., Müller, M., Baumgarten, G., and Konopka, P.: Polar stratospheric cloud observations by MIPAS on ENVISAT: detection method, validation and analysis of the northern hemisphere winter 2002/2003, Atmos. Chem. Phys., 5, 679-692, doi:10.5194/acp-5-679-2005, 2005a.

Spang, R., Remedios, J. J., Tilmes, S., and Riese, M., MIPAS observation of polar stratospheric clouds in the Arctic 2002/2003 and Antarctic 2003 winters, Adv. Space Res., 36, pp.868–878, 2005b.

Spang, R., Griessbach, S., Höpfner, M., Dudhia, A., Hurley, J., Siddans, R., Waterfall, A., Remedios, J. J., Sembhi., H., Technical Note: Retrievability of MIPAS cloud parameter, ESA-ESRIN Contract No. 20601/07/I-OL, March, 2008.

Spang, R., Arndt, K., Dudhia, A., Griessbach, S., Höpfner, M., Hurley, J., Remedios, J. J., Sembhi, H., and Siddans, R., Algorithm Technical Basis Document: Cloud Information Retrieval from MIPAS measurements, ESA-ESRIN Contract No. 20601/07/I-OL, Version 2.1, June 10, 2010a.

Spang, R., M. Höpfner, A. Dudhia, R. Siddans, A. Waterfall, C. Poulsen, J.J. Remedios, H. Sembhi, Product Validation Report for the MIPAS cloud parameter processor, ESA-ESRIN Contract No. 20601/07/I-OL, Version: June 10, 2010b.

Spang, R., Arndt, K., Dudhia, A., Höpfner, M., Hoffmann, L., Hurley, J., Grainger, R. G., Griessbach, S., Poulsen, C., Remedios, J. J., Riese, M., Sembhi, H., Siddans, R., Waterfall, A., and Zehner, C.: Fast cloud parameter retrievals of MIPAS/Envisat, Atmos. Chem. Phys., 12, 7135–7164, doi:10.5194/acp-12-7135-2012, 2012.

Spang, R., Günther, G., Riese, M., Hoffmann, L., Müller, R., and Griessbach, S.: Satellite observations of cirrus clouds in the Northern Hemisphere lowermost stratosphere, Atmos. Chem. Phys., 15, 927-950, doi:10.5194/acp-15-927-2015, 2015.

Stiller, G. P. (Ed.): The Karlsruhe Optimized and Precise Radiative Transfer Algorithm (KOPRA), vol. FZKA 6487 of Wissenschaftliche Berichte, Forschungszentrum Karlsruhe, 2000.

Toon, O. B., Tolbert, M. A., Middlebrook, A. M., and Jordan, J.: Infrared optical constants of H2O, ice, amorphous nitric acid solutions, and nitric acid hydrates, J. Geophys. Res., 99, 25 631-25 654, 1994.

Weigel, R., Volk, C. M., Kandler, K., Hösen, E., Günther, G., Vogel, B., Grooß, J.-U., Khaykin, S., Belyaev, G. V., and Borrmann, S.: Enhancements of the refractory submicron aerosol fraction in the Arctic polar vortex: feature or exception?, Atmos. Chem. Phys., 14, 12319-12342, doi:10.5194/acp-14-12319-2014, 2014.

Winker, D. M., et al.: Overview of the CALIPSO Mission and CALIOP Data Processing Algorithms, J. Atmos. Ocean. Tech., 26, 2310–2323, doi:10.1175/2009JTECHA1281.1, 2009.

WMO (World Meteorological Organization): Scientific Assessment of Ozone Depletion 2014, World Meteorological Organization, Global Ozone Research and Monitoring Project-Report No. 55, 416 pp., Geneva, Switzerland, 2014.